Commun Nonlinear Sci Numer Simulat 47 (2017) 48–70

Contents lists available at ScienceDirect

Commun Nonlinear Sci Numer Simulat

journal homepage: www.elsevier.com/locate/cnsns

Research paper

Geometry of escaping dynamics in nonlinear ship motion

Shibabrat Naik*, Shane D. Ross

Engineering Mechanics Program, Department of Biomedical Engineering & Mechanics, Virginia Tech, Blacksburg, VA-24061, USA

ARTICLE INFO

Article history:
Received 21 September 2016
Revised 27 October 2016
Accepted 28 October 2016
Available online 10 November 2016

Keywords:
Invariant manifolds
Escaping dynamics
Ship capsize
Rough seas

ABSTRACT

Escape from a potential well is a paradigm to understand critical events in chemical physics, celestial mechanics, structural mechanics, and ship dynamics, to name but a few. The consequences of escape could be desirable or undesirable depending on the specific problem at hand, however, the general question is how escape occurs and the effects of environmental noise on the escape. In this article, we answer the first question by discovering the phase space structures that lead to escape and the second question by investigating the effects of random forcing on these structures in the context of ship dynamics and capsize. The phase space structures that lead to escape are the tube manifolds associated to the rank-1 saddles in the conservative system. They are also robust in the sense of predicting high probability regions of escape even in the presence of random forcing.

1. Introduction

Ship dynamics and modeling. Since ancient times ships have remained a crucial element in all arenas of life and society and hence the problem of ship capsize has received considerable attention to avoid catastrophe while out at sea. Initially, this problem was tackled assuming a linear response, and stability of a ship was analyzed under steady state assumptions. However, the results from linear analysis only remain true for small amplitude motion and underestimate the critical conditions leading to capsize, which are primarily large amplitude, complicated nonlinear phenomena [1]. The primary objectiv\e of analyzing such models for different sea states is to generate initial conditions that lead to imminent capsize, or predict a range of parameter values that should be avoided to retain stability [2]. These models are typically analyzed using the computational and semi-analytical approaches that use the geometric features of the phase space such as the *basin of attraction*, and *basin boundary*. These concepts give rise to tools for analyzing ship capsize, such as the *transient capsize diagram*, the *index of capsizability*, and *integrity measure* [3]. The major traction for these concepts and tools is that they are conceptually simpler for obtaining initial conditions leading to capsize, and they also provide realistic prediction of transient behavior of capsize via the fractal like structure of the basin boundary as opposed to steady state analysis. For design engineers, this approach can serve as a first step towards a comprehensive investigation using either physical model tests or extensive numerical solutions of coupled fluid-vessel models. Furthermore, for control engineers, the geometric view point provides critical regions in the phase space that should be avoided for safety in rough seas.

Capsize criteria and analysis. Typically, a ship's static stability is governed by the GZ-curve which is dependent on the heel angle and provides a measure of the restoring moment experienced by the ship when disturbed from its equilibrium position. Hence, stability analysis based on the GZ-curve is an important first step for ship design. But this analysis ignores the nonlinear coupling with other dynamic degrees of freedom which are significant near capsize, for example, roll-pitch,

* Corresponding author.
E-mail address: shiba@vt.edu (S. Naik).

http://dx.doi.org/10.1016/j.cnsns.2016.10.021
1007-5704/

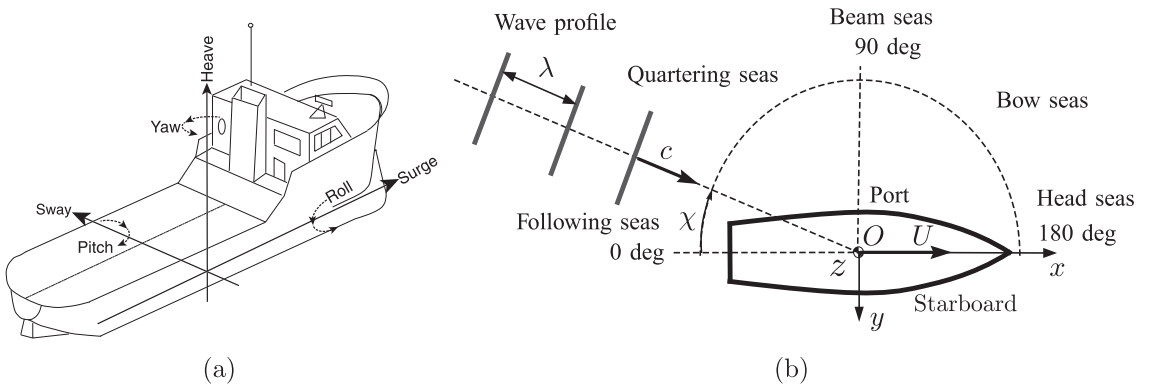

Fig. 1. Schematic adapted from [19] illustrating the wave characteristics relative to ship motion using (x, y, z) as the body-fixed reference frame.

and pitch-heave [4,5]. On the other hand, a complete mathematical model for the motion of a ship includes the six degrees of freedom (associated with a rigid body and as shown in Fig. 1(a)) coupled with the fluid dynamics of the sea. This description of the capsize problem gives rise to an infinite dimensional model (or high dimensional reduced order model) which challenges the identification of critical behavior leading to capsize. Hence, a middle ground of using multi-degree of freedom model that is simple and low dimensional for geometric analysis, but still captures the nonlinear behavior near capsize, will lead to reliable criteria.

Roll-pitch nonlinear coupling. It was observed as early as 1863, by William Froude, that a ship's roll response shows undesirable behavior due to autoparametric resonance when the pitch natural (free oscillation) frequency is twice that of roll natural frequency. To explain this observation, Ref. [6] first proposed that pitch motion can be modeled as a simple harmonic oscillator which then substituted in the roll equation results in a Mathieu-type equation. Thus, this model assumed that pitch affects roll dynamics just as an amplitude-frequency dependent parameter causes resonance in the Mathieu equation. Although this explained the observed parametric response, it also showed exponential instabilities that resulted from not considering the effect of roll on pitch dynamics. However, a more successful attempt at modeling the pitch and roll coupling which is crucial for capsize was proposed in Refs. [7,8], and explored further in Ref. [9]. In this model, the coupling is introduced using a bilinear term in the equation of motion for roll, and via a quadratic term in the equation of motion for pitch. Even with this simple form of nonlinearity, the authors in Refs. [7–9] present an explanation for the undesirable roll motion and various roll-pitch resonance phenomena. The couplings of multiple state variables can significantly alter predictions of safety versus capsize, as emphasized in Refs. [10,11]. Considering the success of the coupled roll-pitch model in predicting observed behavior, we adopt this model for analyzing the large amplitude motions in terms of the geometric view of the phase space for understanding ship capsize in rough seas. Thus, we attempt to introduce conceptual aids for multi-degree of freedom systems which help in systematic interpretation of dynamics that lead to capsize.

Geometric view and escaping dynamics. The main goal in studying capsize of a ship is to obtain initial conditions that lead to undesirable roll motion in the presence of waves. This can be done by performing capsize runs in laboratory experiments of dynamically similar test models [12] along with the prediction of response from the mathematical model. This is where taking a geometric view of the phase space for identifying capsize becomes insightful. First, this approach provides a *skeleton* on which the forced dynamics is built, and provides a classification of orbits that lead to imminent capsize. Secondly, one can use this understanding to provide control strategies in presence of wave forcing. This is done by uncovering the potential energy underlying the coupled roll-pitch motion and then using it in the context of escaping dynamics [13] or escape from a potential well which treats the motion as either bounded or unbounded. Furthermore, the theory of invariant manifolds reveals the pathways in phase space that form the skeleton, even in the presence of random forcing. Thus, the present study aims to adopt the nonlinear coupling of roll-pitch motion as an application of escaping dynamics and invariant manifolds, laying the foundation for a new approach to the avoidance of capsize. More general applications to avoidance of escape in multi-degree of freedom systems can be made.

2. Description of coupled roll-pitch model

We consider the dynamics of the nonlinear coupling of the roll and pitch degrees of freedom of a ship that results in a 4-dimensional phase space of roll, pitch, roll velocity and pitch velocity. The two degree of freedom coupled roll-pitch system has received some attention using perturbation analysis [7–9,14,15]. However, we adopt a global geometric approach of the motion analysis, using techniques which have been successful in celestial mechanics and physical chemistry [16–18]. We start by describing the system in terms of Lagrange's equations of motion and then re-scaling the system appropriately to recast it into a form with the fewest parameters.

2.1. Equations of motion: Lagrangian approach

Based on Refs. [7–9], we consider the coupled roll and pitch equations of the form

$$I_{xx}\ddot{\phi} = -K_\phi\phi - K_{\phi\theta}\phi\theta + \tau_\phi(t)$$
$$I_{yy}\ddot{\theta} = -K_\theta\theta - \frac{1}{2}K_{\phi\theta}\phi^2 + \tau_\theta(t)$$

where, ϕ and θ are roll and pitch angles (in radians), I_{xx} and I_{yy} are the sums of the second moments of inertia and hydrostatic inertia, K_ϕ and K_θ are the linear rotational stiffness related to square of the corresponding natural frequency, $K_{\phi\theta}$ is the nonlinear coupling coefficient. Further, $\tau_\phi(t)$ and $\tau_\theta(t)$ are generalized time-dependent torques in the roll and pitch directions, respectively, which do not necessarily arise from an effective potential energy (for example, damping and wind/wave forcing). These equations are equivalent to Lagrange's equations with the Lagrangian given by

$$\begin{aligned}\mathcal{L}(\phi,\theta,\dot{\phi},\dot{\theta}) =& \mathcal{T}(\dot{\phi},\dot{\theta}) - \mathcal{V}(\phi,\theta)\\ =& \left(\frac{1}{2}I_{xx}\dot{\phi}^2 + \frac{1}{2}I_{yy}\dot{\theta}^2\right) - \left(\frac{1}{2}K_\phi\phi^2 + \frac{1}{2}K_\theta\theta^2 + \frac{1}{2}K_{\phi\theta}\phi^2\theta\right)\end{aligned}$$

and the kinetic and potential energy denoted by $\mathcal{T}(\dot{\phi},\dot{\theta})$, and $\mathcal{V}(\phi,\theta)$, respectively, and generalized non-conservative forces $\tau_\phi(t)$ and $\tau_\theta(t)$. The resulting Lagrange's equations of motion can be recast into a form

$$\begin{aligned}\ddot{\phi} &= -\omega_\phi^2\phi + 2K_1\phi\theta + m_\phi(t)\\ \ddot{\theta} &= -\omega_\theta^2\theta + K_1\frac{I_{xx}}{I_{yy}}\phi^2 + m_\theta(t)\end{aligned} \tag{1}$$

where the coefficients are

$$\omega_\phi = \sqrt{\frac{K_\phi}{I_{xx}}},\ \omega_\theta = \sqrt{\frac{M_\theta}{I_{yy}}},\ K_1 = -\frac{K_{\phi\theta}}{2I_{xx}},\ m_\phi(t) = \frac{\tau_\phi(t)}{I_{xx}},\ m_\theta(t) = \frac{\tau_\theta(t)}{I_{yy}}$$

Rescaled equations of motion. The conservative dynamics, when $m_\phi(t) = m_\theta(t) = 0$, of the system (1) is dependent on four parameters: the natural roll frequency (ω_ϕ), the natural pitch frequency (ω_θ), the nonlinear coupling constant (K_1), and the ratio of second moments of inertia (I_{xx}/I_{yy}). The conservative system has saddle equilibrium points at ($\pm\,\phi_e$, θ_e), where

$$\phi_e = \frac{\omega_\phi\omega_\theta}{K_1\sqrt{2}}\sqrt{\frac{I_{yy}}{I_{xx}}}, \qquad \theta_e = \frac{\omega_\phi^2}{2K_1}$$

and ϕ_e is also called the roll angle of vanishing stability and θ_e is the corresponding pitch angle. The coordinates of saddle equilibrium points (roll and pitch angles of vanishing stability) can now be used to rescale the original (ϕ, θ) coordinates to a nondimensional set (x, y). Furthermore, the natural roll frequency can be used as the time scale to obtain nondimensional time, $\bar{t}$. We define

$$x = \frac{\phi}{\phi_e}, \qquad y = \frac{\theta}{2\theta_e}, \qquad \bar{t} = \omega_\phi t \tag{2}$$

and the equations of motion (1) become

$$\begin{aligned}\mathring{x} &= -x + 2xy + f_x(\bar{t})\\ \mathring{y} &= -R^2y + \frac{1}{2}R^2x^2 + f_y(\bar{t})\end{aligned} \tag{3}$$

where $\mathring{(\cdot)}$ denotes the time derivative with respect to the nondimensional time, $\bar{t}$ and $R = \omega_\theta/\omega_\phi$ denotes the ratio of pitch to roll natural frequencies as the only system parameter for the conservative dynamics. From now on, we will drop the bar on $\bar{t}$ and rescaled time will be understood. These are Lagrange's equations of motion with rescaled Lagrangian

$$L(x,y,\mathring{x},\mathring{y}) = \frac{1}{2}\mathring{x}^2 + \frac{1}{2}\left(\frac{2}{R^2}\right)\mathring{y}^2 - \left(\frac{1}{2}x^2 + y^2 - x^2y\right) \tag{4}$$

where the rescaled potential energy is given by

$$V(x,y) = \frac{1}{2}x^2 + y^2 - x^2y \tag{5}$$

which is independent of the only system parameter, R, and is shown graphically in Fig. 2(a). The rescaling of the coordinates and time has made the nonlinear coupling term of the potential into unity and the original coordinates can always be recovered using the transformation (2). We note that Eq. (3) are identical to those derived by Ref. [20], where they were called *symmetric internal resonance* equations. The potential energy (5) is also similar to the Barbaris potential studied by the chemistry community [13,21,22].

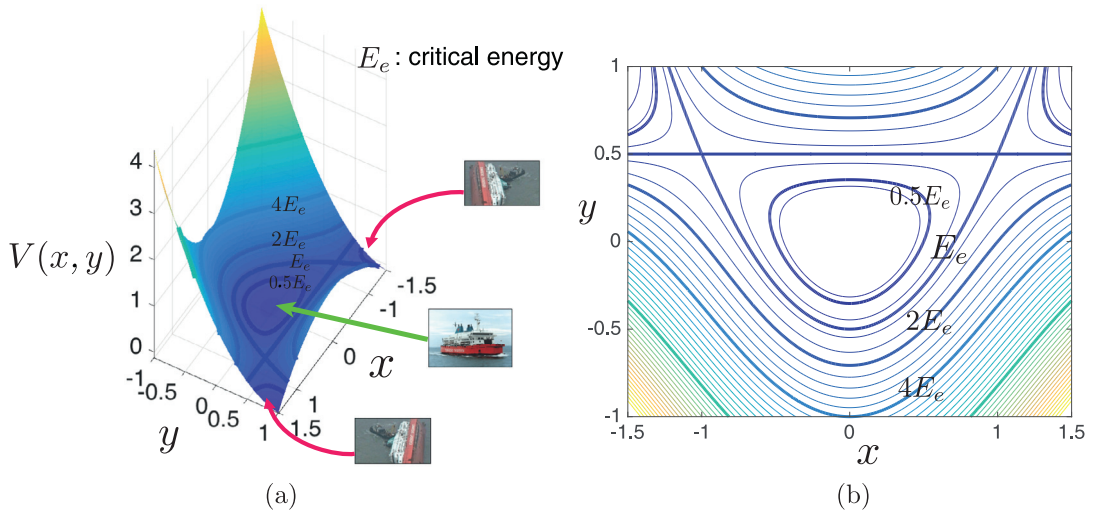

Fig. 2. (a) Shows the effective potential energy with an upright ship in the region that corresponds to bounded motion inside the well and a capsized ship in the region that corresponds to unbounded motion. The total energy of the system can be considered as fixing a height of this potential well and shown here as contour lines of $0.5E_e$, E_e, $2E_e$, $4E_e$. (b) Shows the total energy as contour lines on the configuration space (x, y) for different values above and below the critical energy E_e.

Conservative form. The equation of motion in the absence of damping and forcing ($f_x(t) = f_y(t) = 0$) can be expressed in first order form as

$$\begin{aligned} \dot{x} &= v_x \\ \dot{y} &= v_y \\ \dot{v}_x &= -x + 2xy \\ \dot{v}_y &= -R^2 y + \frac{1}{2}R^2 x^2 \end{aligned} \tag{6}$$

which conserves the total energy

$$E(x, y, v_x, v_y) = \frac{1}{2}v_x^2 + \frac{1}{R^2}v_y^2 + \frac{1}{2}x^2 + y^2 - x^2 y \tag{7}$$

Non-conservative form. Any non-potential and time-varying generalized forces $(f_x(t), f_y(t))$ on the right hand side of (8)

$$\begin{aligned} \dot{x} &= v_x \\ \dot{y} &= v_y \\ \dot{v}_x &= -x + 2xy + f_x(t) \\ \dot{v}_y &= -R^2 y + \frac{1}{2}R^2 x^2 + f_y(t) \end{aligned} \tag{8}$$

can be written in terms of the original angular accelerations $(m_\phi(t), m_\theta(t))$, that is,

$$f_x(t) = \frac{K_1}{\omega_\phi^4}\frac{\sqrt{2}}{R}\sqrt{\frac{I_{xx}}{I_{yy}}}m_\phi(t), \qquad f_y(t) = \frac{K_1}{\omega_\phi^4}m_\theta(\bar{t}) \tag{9}$$

When $f_x(t)$ and $f_y(t)$ are non-zero, the total energy changes with time according to

$$\dot{E} = v_x f_x(t) + \frac{2}{R^2}v_y f_y(t) = \langle \mathbf{v}, \mathbf{f} \rangle \tag{10}$$

where $\langle\cdot\rangle$ denotes the dot product of the velocity vector, $\mathbf{v} = (v_x, v_y)$, and the augmented force vector, $\mathbf{f} = (f_x, (2/R^2)f_y)$. This energy evolution equation acts as the constraint on how quickly the dynamics can qualitatively change and go from below the critical energy (energy of the saddle points) to above when capsize is possible. In particular, if we consider including any damping forces linear in $\mathbf{v}$ of the form

$$f_i = -k(x, y, v_x, v_y)v_i \qquad \text{where,} \quad k(x, y, v_x, v_y) \geqslant 0 \tag{11}$$

then such forces can only lead to a decrease in energy while a generalized time-dependent forcing, in particular an arbitrary signal $f_i(t)$, such as encountered during random waves, can lead to increase or decrease in energy. We should note here that in the non-conservative form, energy can still be kept constant if the velocity vector (v_x, v_y) is orthogonal to $(f_x, (2/R^2)f_y)$.

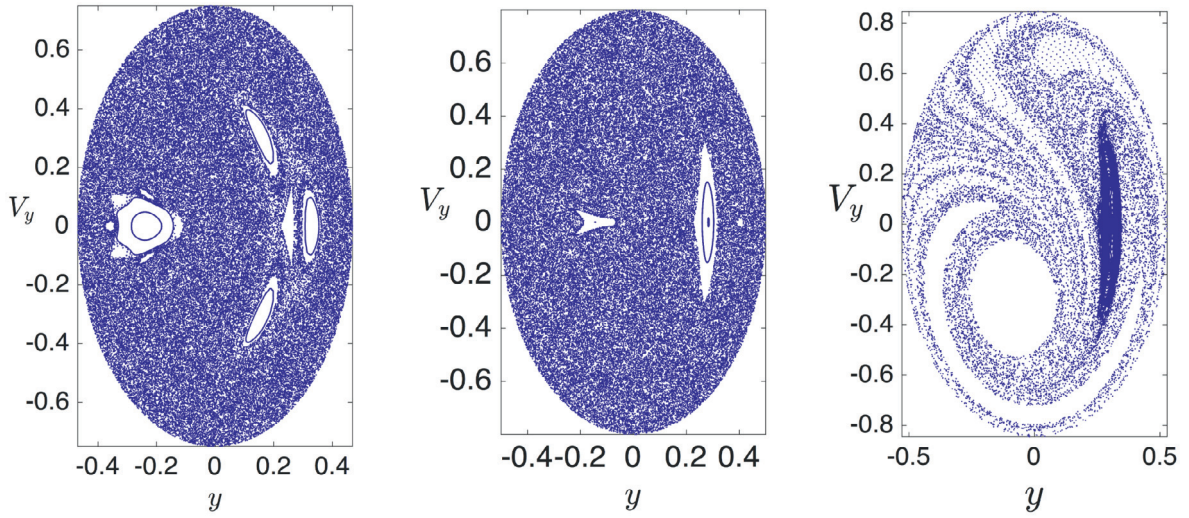

Fig. 3. Poincaré surface-of-section (SOS) of the energy surface, showing orbits of the return map for different energy values. In the absence of damping and wave forcing, the system conserves energy and for energy below the critical value, E_e, all the trajectories intersect the SOS (13) as shown in (a) and (b) for $e = 0.22$ and $e = 0.25$. When the energy is above the critical value, trajectories leading to capsize do not intersect the surface (13) any longer and hence less return orbits are shown in (c).

2.2. Energy surface

Let $\mathcal{M}(e)$ be the energy surface given by setting the integral (7) equal to a constant, i.e.,

$$\mathcal{M}(e) = \{(x, y, v_x, v_y) | E(x, y, v_x, v_y) = e\} \tag{12}$$

where e denotes the constant value of energy. For a fixed energy e, one can consider the surface $\mathcal{M}(e)$ as a three-dimensional surface embedded in the four-dimensional phase space, $\mathbb{R}^4$ and thus, co-dimension 1. Furthermore, if we take a cross-section of this three-dimensional surface, we obtain a two-dimensional Poincaré surface-of-section (SOS). The SOS can be used to define a two-dimensional return map ($\mathbb{R}^2 \to \mathbb{R}^2$) for a constant energy, e. This is shown for successively increasing energy in Fig. 3, and $R = 1.6$, for the SOS defined as

$$U_1 = \{(y, v_y) | x = 0, v_x(y, v_y; e) > 0\}, \qquad \text{motion to the right} \tag{13}$$

$$U_2 = \{(y, v_y) | x = 0, v_x(y, v_y; e) < 0\}, \qquad \text{motion to the left} \tag{14}$$

where, $v_x > 0$ is used to enforce a directional crossing of the surface. The energy of the equilibrium points is called the critical energy (or escaping energy) which is given by $E_e = 0.25$. As the trajectories approach this energy from below, capsize becomes inevitable and this can be interpreted in terms of the potential energy well. Since the potential energy (5) is independent of any system parameter, the discussion based on this potential well will be more general.

2.2.1. Potential well and critical energy

We recall that the total energy (7) of the conservative system can be fixed at a constant value, i.e., $E(x, y, v_x, v_y) = e$, and this is equivalent to fixing a height in the plot of the effective potential, $V(x, y)$. Considering the configuration space, (x, y), projection of effective potential in Fig. 2(b), we note that there are two equilibrium points (they are rank-1 saddles, as we will show later) in the (x, y) plane at $(\pm 1, 1/2)$ which are symmetrically located about the y-axis. Furthermore, the total energy of the system can be shown as a height on the potential surface and for a conservative system all possible states can only explore the surface below this value. For example, we show the contour lines of $0.5E_e$, E_e, $2E_e$, $4E_e$ in Fig. 2(a) and (b). Thus, the critical energy divides the motion into two energy cases which can simplify the understanding even when forcing is added.

1. **Case 1**, $E(x, y, v_x, v_y) < E_e$: If the energy is below E_e, the ship is safe against capsize as the state can not move from the region of bounded motion (surrounding the origin) to the region of unbounded motion i.e., capsize (beyond the saddles). See Fig. 4(a)
2. **Case 2**, $E(x, y, v_x, v_y) > E_e$: If the energy is just above E_e, two "bottlenecks" between the region of unbounded motion and bounded motion open up around the saddle points, permitting trajectories to move between the two realms. We will show in the next section that the transport through the bottlenecks connecting the two adjacent regions is controlled by invariant manifolds associated with the saddle points. See Fig. 4(c)

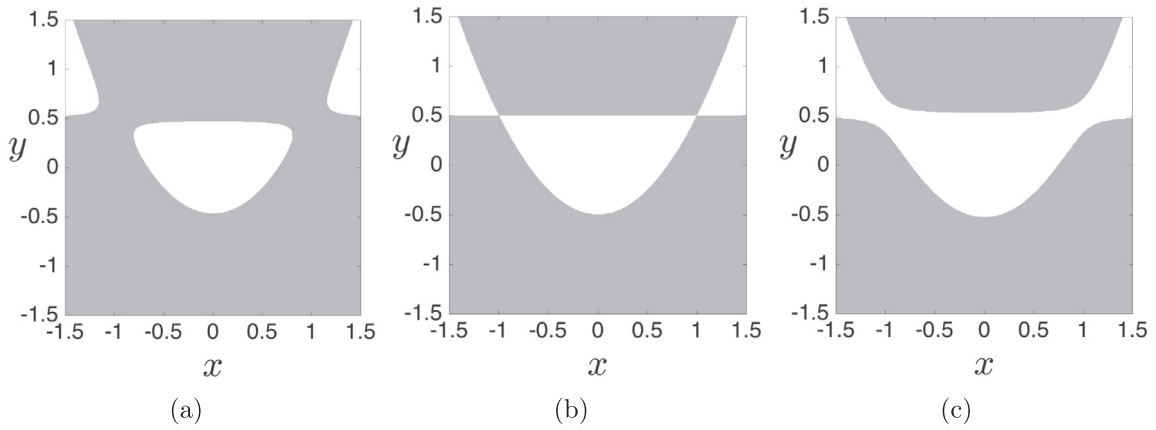

Fig. 4. (a), (b), and (c) show the Hill's region for $e < E_e$, $e = E_e$, and $e > E_e$ where E_e denotes the critical energy. The white region is the energetically accessible region bounded by the zero velocity curve and while the gray region is the energetically forbidden realm where kinetic energy is negative and motion is impossible.

2.2.2. Hill's region and zero velocity curve

The projection of energy surface into configuration space, (x, y) plane, is the region of energetically possible rolling and pitching motion of a ship of energy e. Let $M(e)$ denote this projection defined as

$$M(e) = \{(x, y) | V(x, y) \leqslant e\} \tag{15}$$

where $V(x, y)$ is the potential energy as in (5). The projection (15) of energy surface is known historically in mechanics as the *Hill's region*. The boundary of $M(e)$ is known as the *zero velocity curve*, and plays an important role in placing bounds on the ship's motion for a given energy. The zero velocity curves are the locus of points in the (x, y) plane where the kinetic energy, and hence the angular velocity vector vanishes, that is

$$E(x, y, v_x, v_y) = e = \frac{1}{2}\left(v_x^2 + \frac{2}{R^2}v_y^2\right) + V(x, y) \tag{16}$$

$$v_x^2 + \frac{2}{R^2}v_y^2 = 2(e - V(x, y)) = 0 \tag{17}$$

From (15), it is clear that the ship's state is only able to move on the side of this curve for which the kinetic energy is positive. The other side of the curve, where the kinetic energy is negative and motion is impossible, will be referred to as the *energetically forbidden realm*.

2.3. Symmetries of the conservative equations of motion

We note the symmetries in the conservative system (6), when $f_x = 0$ and $f_y = 0$, by substituting $(-x, -v_x)$ for (x, v_x) which implies reflection about the $y-$axis and expressed as

$$s_x : (x, y, v_x, v_y, t) \to (-x, y, -v_x, v_y, t) \tag{18}$$

Thus, if $(x(t), y(t), v_x(t), v_y(t))$ is a solution to (6), then $(-x(t), y(t), -v_x(t), v_y(t))$ is another solution. The conservative system also has time-reversal symmetry

$$s_t : (x, y, v_x, v_y, t) \to (x, y, -v_x, -v_y, -t) \tag{19}$$

So, if $(x(t), y(t), v_x(t), v_y(t))$ is a solution to (6), then $(x(-t), y(-t), -v_x(-t), -v_y(-t))$ is another solution. These symmetries can be used to decrease the number of computations, and to find special solutions. For example, any solution of the conservative system will move so as to keep the energy E given by (7) constant. For fixed energy, there will be zero velocity curves corresponding to $V(x, y) = e$, the contours shown in Fig. 2(b). Any trajectory which touches the zero velocity curve at time t_0 must retrace its path in configuration space (i.e., $q = (x, y)$ space),

$$q(-t + t_0) = q(t + t_0) \qquad \dot{q}(-t + t_0) = -\dot{q}(t + t_0) \tag{20}$$

We note that $y = v_y = 0$ is not an invariant manifold of the system, due to the nonzero coupling term (i.e., $K_1 = 0$), so no pure motion in roll (ϕ) is possible. However, $x = v_x = 0$ is an invariant manifold, so pure motion in pitch (θ) is possible.

3. Invariant manifolds and ship capsize

3.1. Conservative dynamics

Tubes and transport. The global geometric view of capsize of a ship is to say the trajectories will escape the potential well for energy states above the critical energy. This has been known as *escaping dynamics* [13] and can be systematically understood using invariant manifolds which act as pathways for switching between capsize and non-capsize regions of the phase space. When the phase space is $\mathbb{R}^4$, as in the dynamical system considered here, the stable and unstable manifolds of a periodic orbit on the energy surface are codimension-1 in the energy surface and topologically equivalent to $\mathbb{S}^1 \times \mathbb{R}^1$. Due to this cylindrical geometry, they are referred to as *cylindrical manifolds or tubes* [23] and the geometric framework they imply as *tube dynamics*. The physical property of the tube manifold is that all motion that crosses a saddle equilibrium point must occur through the interior of the corresponding tube manifold. Thus, the global transport of states between the capsize and non-capsize realms in the phase space is mediated by the tubes.

Numerical approach. The invariant manifolds are global objects in the sense that they exist in the entire phase space and can be numerically computed for infinite time. However, the invariant manifolds are associated with the unstable periodic orbits in the equilibrium regions around each saddle. This poses two challenges for the computation: saddle directions cause periodic orbit to be unstable, and exponential separation of trajectories on the manifolds. Hence, we need approaches that use the linearized behavior near the equilibrium points to generate the geometric structure of manifolds, and target periodic orbits of specified energy. This is where the theory of invariant manifolds of a periodic orbit and numerical approach of globalization of manifolds can be useful.

We adopt the numerical method for computing periodic orbits restricted to a specified energy from Ref. [23], however, a more general method applicable to higher dimensional systems is computing the center manifold associated with the saddle as in Ref. [24]. The main idea of the numerical approach is to obtain a guess for the initial condition on the periodic orbit by using the eigenvector in the center direction of the saddle equilibrium point. Then, using this initial guess a shooting type numerical procedure called *differential correction* is performed to correct the initial guess. This shooting and correcting process is done iteratively with a specified tolerance ($\approx 10^{-8}$) until the initial condition for a periodic orbit of small amplitude ($\approx 10^{-4}$) is obtained. Then we begin the targeting step which aims for a specified energy of the periodic orbit using *numerical continuation* and successively increases the amplitude of the periodic orbit until the tolerance for energy of the orbit is satisfied.

3.1.1. Algorithm for computing tube manifolds leading to imminent capsize

In this section, we go through the steps of computing tube manifolds that lead to imminent capsize.

Step 1: Select an appropriate energy. We begin by deciding and selecting the total energy of the ship at an initial instant and in absence of forcing, this total energy (7) is conserved. Depending on whether the instantaneous energy is above or below the critical value, E_e, the bottleneck around the equilibrium points either exist or do not exist. For the purpose of our computations, we use values of $E = 0.253, 0.28$ or $\Delta E = 0.003, 0.03$, respectively, where $\Delta E = E - E_e$, which correspond to energy at which bottlenecks exist and tubes lead to imminent capsize. Furthermore, we will see in the following discussion that the magnitude of ΔE is related to the width of the bottleneck and hence is very relevant to the number of trajectories that lead to capsize.

Step 2: Compute the periodic orbit about the critical point of interest. Next, we analyze the linearized dynamics near the saddle equilibrium points which extends to the full nonlinear system due to the generalization of Lyapunov's theorem by [25]. On one hand this analysis simplifies the types of orbits that exist in the full phase space (see Appendix B for details) and on the other hand, this is also a straightforward procedure to compute periodic orbits around the equilibrium points. We compute the non-trivial equilibrium points for the conservative form of the system at (±1, 0.5, 0, 0). In the present discussion, we will generally denote the left and right equilibrium points by (x_e, y_e, 0, 0) and call them as C_1 and C_2, respectively, for specific notation.

Obtain guess for initial condition. The stability of these equilibrium point can be obtained by linearizing the system about it and computing the eigenvalues. This computation is shown in Appendix B and we obtain eigenvalues (B.3) of the form $\pm\lambda$ and $\pm i\nu$. The complex eigenvalue and its corresponding eigenvector can now be used to generate a guess for initial condition on the periodic orbit and its period T, which will be close to $2\pi/\nu$. Next, considering the saddle equilibrium point, C_2, we construct the initial condition using the general solution (B.8) of the linearized system (B.1). The initial conditions of a periodic orbit (p.o.) of x−amplitude $A_x > 0$ can be computed by letting $t = \alpha_1 = \alpha_2 = 0$ and $\beta = -A_x/2$. This is now transformed back into the original coordinates and yields an initial condition

$$\tilde{x}_0 = \left(1, \frac{1}{2}, 0, 0\right) + 2Re(\beta w_1) \tag{21}$$

where $\beta = A_x/2$ is a small amplitude. Thus, using the formula (B.6) we obtain the initial guess as

$$\tilde{x}_0 = \left(1 + A_x, \frac{1}{2} + \frac{A_x R^2}{R^2 - \nu^2}, 0, 0\right) \tag{22}$$

Differential correction and numerical continuation. Now, with the guess for initial condition in hand, we consider a shooting method for computing the periodic orbits around C_2 (and equivalently C_1). This approach begins with small "seed"

periodic orbits obtained from the linearized equations of motion near C_2, and uses differential correction and numerical continuation to generate the desired p.o. corresponding to the selected energy, e. The initial condition given in (22) will only yield a good approximation to a p.o. in the nonlinear equations (6) in the case $A_x < <1$ which corresponds to a much smaller energy than we selected in step 1. For the p.o. corresponding to the selected energy, e, the amplitude is larger than A_x and thus to obtain such an amplitude, we proceed as follows. Let $A_{x_1} < A_{x_2} << 1$ be two small amplitudes with corresponding guess initial conditions $\bar{x}_{0,g}^{(1)}$ and $\bar{x}_{0,g}^{(2)}$, respectively, where g denotes that this is an initial guess to a true periodic solution of (6).

We will use differential correction, described in Appendix D, to produce initial condition that converge to a periodic orbit of energy e in the nonlinear equations which are accurate to some specified tolerance d. The convergence criteria is based on the property of a periodic orbit that it returns to the starting point after a given period. The computation of periodic orbits and the corresponding period, for general time-dependent nonlinear systems, is a numerical field in its own right but we can use the knowledge of the center subspace to initialize a shooting type procedure. Thus, if $\bar{x}_{po} \equiv \bar{x}_0$ is a true initial condition on a p.o., $x_{po}(t)$, of period T, the convergence criteria requires

$$\|\bar{x}_{po}(T) - \bar{x}_{po}(0)\| < d \tag{23}$$

for a specified tolerance, $d \approx 10^{-6}$. Differential correction uses the analytical expression of the first guess in an iterative process which shoots for the end point, checks the error and updates the initial condition while keeping some values constant. In our case, we want to keep the x-value constant and update the y-value of the guess initial condition for the periodic orbit. Thus, the correction term (see Appendix D for derivation) is given by

$$\delta y_0 = \left(\Phi_{32} - \Phi_{42}\frac{\dot{v}_{x_1}}{\dot{v}_{y_1}}\right)^{-1} v_{x_1}$$

and hence to satisfy the tolerance on v_{x_1}, we let

$$y_0 \to y_0 - \delta y_0$$

This process of adding *small corrections*, hence the name differential correction, converges to $|v_{x_1}| < d$ within a few iterations, typically $10-20$ for the tolerance, $d \approx 10^{-10}$. The above procedure yields an accurate initial condition for a periodic orbit from the starting guess. If our initial guess came from a linear approximation near the equilibrium point (B.8), it has been observed numerically that we can only use this procedure for small amplitude around the critical point, C_i, and this corresponds to energy much lower than the critical energy. But for computation of bottlenecks around these critical points, we want an orbit of arbitrarily large amplitude (which is in one-to-one correspondence with the energy e), we resort to numerical continuation to generate the family of periodic orbits which reaches the appropriate energy, e. It is to be noted here that this appropriate energy has to be below a certain upper bound at which bifurcation of the periodic orbits occur [26]. In this present work, we are concerned with a ship rolling with total energy below that upper bound but careful computation of the periodic orbits is needed when the total energy is close to the upper bound.

To this end, we proceed as follows. Suppose we find two small nearby periodic orbit initial conditions, $\bar{x}_0^{(1)}$ and $\bar{x}_0^{(2)}$, correct to within the tolerance d, using the differential correction procedure described above. We can generate a family of periodic orbits with successively increasing amplitudes around C_i in the following way. Let

$$\begin{aligned}\Delta &= \bar{x}_0^{(2)} - \bar{x}_0^{(1)} \\ &= [\Delta x_0, \Delta y_0, 0, 0]^T\end{aligned}$$

A linear extrapolation to an initial guess of slightly larger amplitude, $\bar{x}_0^{(3)}$ is given by

$$\begin{aligned}\bar{x}_{0,g}^{(3)} &= \bar{x}_0^{(2)} + \Delta \\ &= \left[(x_0^{(2)} + \Delta x_0), (y_0^{(2)} + \Delta y_0), 0, 0\right]^T \\ &= \left[x_0^{(3)}, y_0^{(3)}, 0, 0\right]^T\end{aligned}$$

Thus, keeping $x_0^{(3)}$ fixed, we can use differential correction on this initial condition to compute an accurate solution $\bar{x}_0^{(3)}$ from the initial guess $\bar{x}_{0,g}^{(3)}$ and repeat the process until we have a family of solutions. We can keep track of the energy of each periodic orbit and when we have two solutions, $\bar{x}_0^{(k)}$ and $\bar{x}_0^{(k+1)}$, whose energies bracket the appropriate energy, e, we can refine our continuation until we find a periodic orbit of energy e to within a specified tolerance. Thus, the result is a periodic orbit of desired energy e and of some period T with initial condition X_0.

Step 3: Compute the tube manifolds of the periodic orbit. First, we find the local approximation to the unstable and stable manifolds of the periodic orbit from the eigenvectors of the monodromy matrix. Next, the local linear approximation of the unstable (or stable) manifold in the form of a state vector is integrated in the nonlinear equations of motion to produce the approximation of the unstable (or stable) manifolds. This procedure is known as globalization of the manifolds and we proceed as follows:

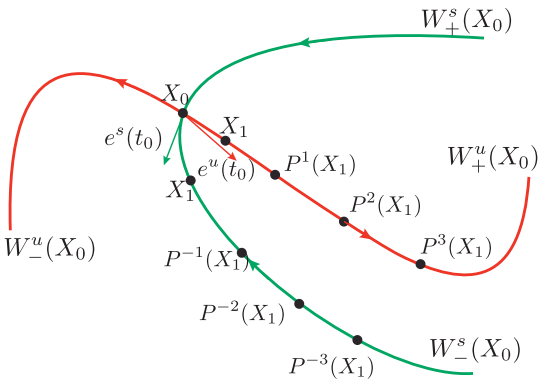

Fig. 5. Schematic of the globalization of invariant manifolds that computes an approximation of the two branches of the unstable ($W^u_\pm$) and stable ($W^s_\pm$) manifolds of a periodic orbit. The two branches are computed using the positive and negative directions of the eigenvectors $e^u(t_0)$ and $e^s(t_0)$, respectively, after an initial displacement of small magnitude from X_0 to X_1. Then, the unstable (stable) manifold is computed using successive forward (backward) iterate of the map P which marches along the half manifold.

First, the state transition matrix $\Phi(t)$ along the periodic orbit with initial condition X_0 can be obtained numerically by integrating the variational equations along with the equations of motion from $t = 0$ to $t = T$. This is known as the monodromy matrix $M = \Phi(T)$ and the eigenvalues can be computed numerically. For Hamiltonian systems (see [27] for details), tells us that the four eigenvalues of M are of the form

$$\lambda_1 > 1, \qquad \lambda_2 = \frac{1}{\lambda_1}, \qquad \lambda_3 = \lambda_4 = 1$$

The eigenvector associated with eigenvalue λ_1 is in the unstable direction, the eigenvector associated with eigenvalue λ_2 is in the stable direction. Let $e^s(X_0)$ denote the normalized (to 1) stable eigenvector, and $e^u(X_0)$ denote the normalized unstable eigenvector. We can compute the manifold by initializing along these eigenvectors as:

$$X^s(X_0) = X_0 + \epsilon e^s(X_0)$$

for the stable manifold at X_0 along the periodic orbit, as illustrated in Fig. 5, and as

$$X^u(X_0) = X_0 + \epsilon e^u(X_0)$$

for the unstable manifold at X_0. Here the small displacement from X_0 is denoted by ϵ and its magnitude should be small enough to be within the validity of the linear estimate, yet not so small that the time of flight becomes too large due to asymptotic nature of the stable and unstable manifolds. Ref. [28] suggests typical values of $\epsilon > 0$ corresponding to nondimensional position displacements of magnitude around 10^{-6}. By numerically integrating the unstable vector forwards in time, using both ϵ and $-\epsilon$, for the forward and backward branches respectively, we generate trajectories shadowing the two branches, W^u_+ and W^u_-, of the unstable manifold of the periodic orbit. Similarly, by integrating the stable vector backwards in time, using both ϵ and $-\epsilon$, for forward and backward branch respectively, we generate trajectories shadowing the stable manifold, $W^s_{+,-}$. This numerical procedure is shown schematically in Fig. 5. For the manifold at $X(t)$, one can simply use the state transition matrix to transport the eigenvectors from X_0 to $X(t)$:

$$X^s(X(t)) = \Phi(t, 0)X^s(X_0)$$

It is to be noted that since the state transition matrix does not preserve the norm, the resulting vector must be normalized.

The globalized invariant manifolds associated with rank-1 saddles are known as Conley–McGehee tubes [29] and give insight into capsize criteria or control of capsize when a generalized wave moment is acting on a ship. These *tubes* form the skeleton of escape dynamics by leading the states inside them to unbounded motion and the states outside to stay bounded in the potential well.

Step 4: Obtain the intersection of Poincaré surface-of-section and the globalized manifolds. We adopt the Poincaré surface-of-sections U_1 and U_2 defined as two-dimensional surfaces in (13) and (14), respectively. In this form, $v_x(y, v_y; e)$ means v_x is constrained by the energy (7) for a trajectory that intersects the surface U_1 with positive v_x (or U_2 with negative v_x). Thus, the Poincaré section acts as a surface on which trajectories leading to capsize can be studied, and this is shown in Fig. 6. The two surfaces differ only in the direction of motion of the trajectories passing through them. The surfaces U_i are strategically placed, allowing us to get cross-sections of the flow within the three-dimensional energy surface $\mathcal{M}(e)$. Referring to the Fig. 7(a), where we use $R = 1.6$ and $\Delta E = 0.03$, if we integrate backwards (in time) the stable manifold of the periodic orbit around the right critical point until it intersects U_1, we obtain an elliptical region that is topologically a circle, $\mathbb{S}^1$, shown in y vs. v_y coordinates. Although the stable manifold does not stop here, being a global object, we know

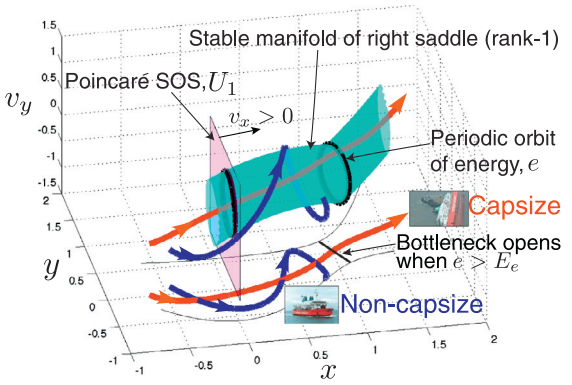

Fig. 6. Shows the Poincaré surface-of-section, U_1 (13), as the magenta plane and the stable manifold of right saddle is shown as the cyan surface for a given energy e. The stable manifold is codimension-1 in the 3-dimensional energy surface and has geometry $\mathbb{R}^1 \times \mathbb{S}^1$ that is cylindrical, and hence the name *tube manifold*. The stable manifold of a saddle up to its first intersection with U_1 is the pathway that leads to imminent capsize. The trajectory that leads to escape from the potential well and corresponds to the imminent capsize of a ship, for example the red trajectory, lies in the interior of the tube. Similarly, a trajectory that stays inside the potential well and corresponds to an upright ship lies outside the tube. These example trajectories are shown in the $x - y - v_y$ space for a given energy e and also as projection in the configuration space. (For interpretation of the references to colour in this figure legend, the reader is referred to the web version of this article.)

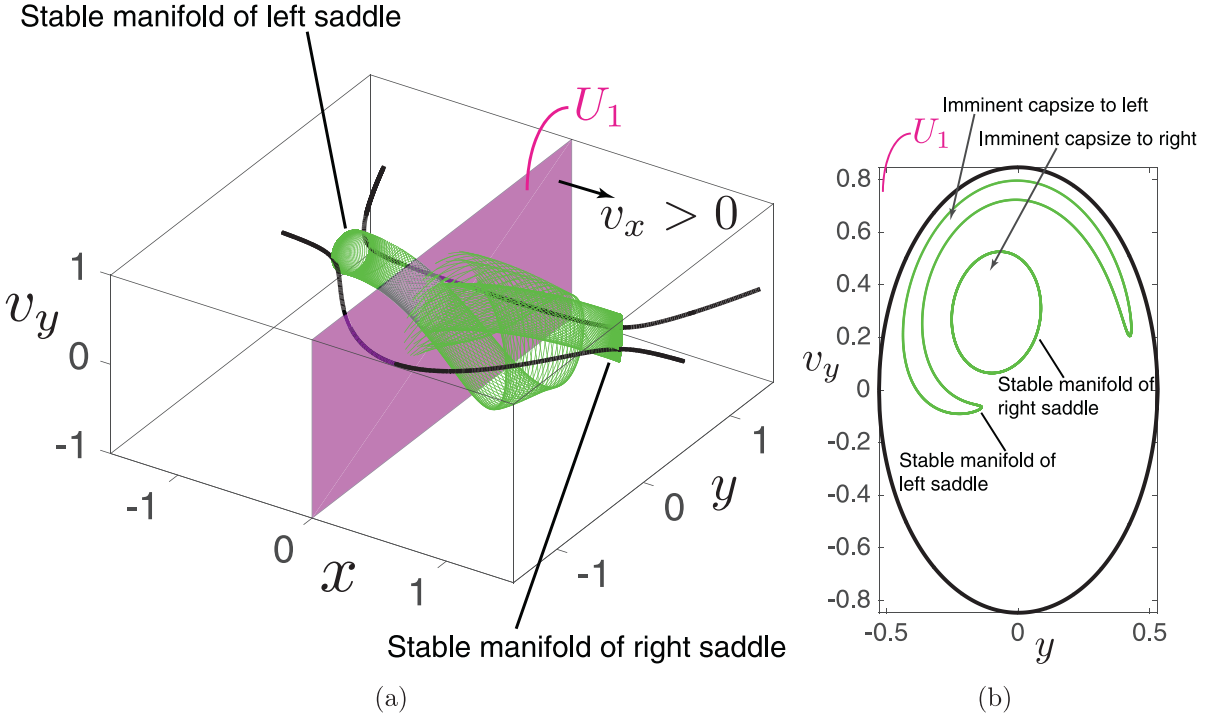

Fig. 7. (a) Shows the tubes that lead to imminent capsize to left and right, and the SOS, U_1 (13), is shown as the magenta plane. These are the stable manifolds of the left and right saddles, and are cylindrical, that is $\mathbb{R}^1 \times \mathbb{S}^1$ geometry. (b) Shows the intersection of the stable manifolds with the SOS U_1 as regions with green boundary, and the black boundary corresponds to intersection of the energy surface (12) with the SOS U_1. where the boundary of the region leading to imminent capsize is the intersection of the stable manifolds with the SOS. (For interpretation of the references to colour in this figure legend, the reader is referred to the web version of this article.)

the initial conditions inside this ellipse will lead to imminent capsize through the bottleneck on the right side. Furthermore, if we pick an initial condition on U_1, but which is outside of this ellipse, and integrate forward, it will not lead to capsize, and will instead 'bounce back' from the neck region, since it a non-transit orbit. It is to noted that for a smaller energy above critical, for example $\Delta E = 0.003$, the tube manifold has a smaller width and its intersection with Poincaré sections has a smaller width and hence its intersection with U_1 is a smaller elliptical region.

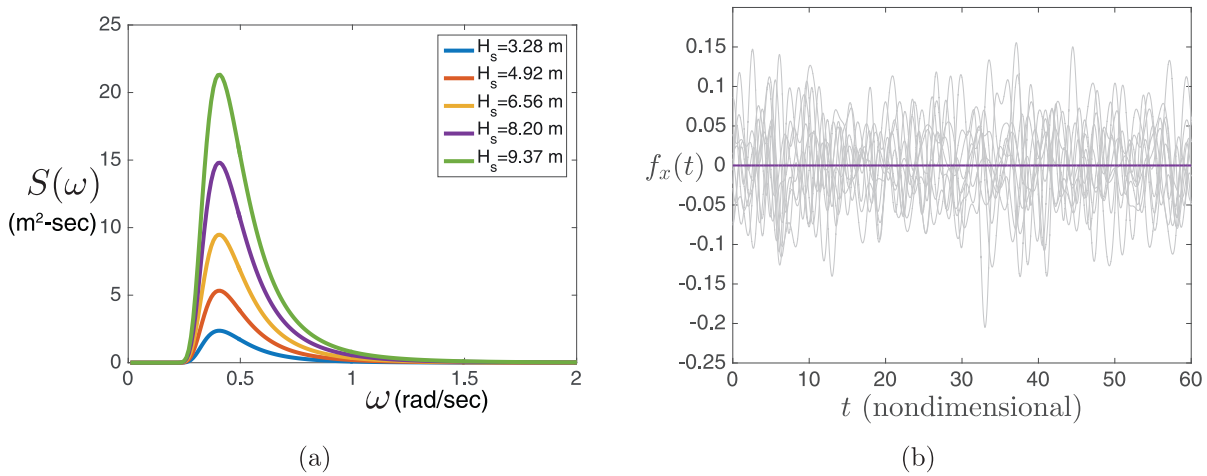

Fig. 8. (a) Shows the wave energy spectrum, called the *Pierson–Moskowitz*, for different significant wave height. The peak energy is centered at th same frequency and the max energy increases with increasing significant wave height. This is used to sample the wave forcing for simulating a ship rolling and pitching in rough sea. (b) Shows 10 samples of forcing, $f_x(t)$ in beam sea of significant wave height, $H_s = 4.92$ m and the mean of 10^5 ensembles as the zero line which demonstrates the underlying stochastic process has zero mean.

3.2. Non-conservative dynamics

Motion in rough sea. Ocean waves are typically modeled as realizations of a stationary and homogeneous Gaussian stochastic process with zero mean [19]. This stochastic process is represented by a standard formula for the power spectral density (PSD) of the sea surface elevation that describes the energy content of the ocean waves distributed over the frequency domain. We adopt the *Pierson–Moskowitz* wave spectrum given by

$$S(\omega) = 0.11 H_s^2 \frac{\omega_z^4}{\omega^5} \exp\left(-0.44\left(\frac{\omega_z}{\omega}\right)^4\right) \tag{24}$$

where $S(\omega)$ is the wave energy spectrum that denotes the PSD for a particular sea environment, H_s is the significant wave height (which is defined as the average of the heights of largest 1/3rd of the waves), $\omega_z = 0.527$ rad/s is the characteristic frequency, ω is the wave frequency. The wave frequency is typically sampled over discrete frequencies over the range $\omega_1 = d\omega$ to $\omega_N = 2$ rad/s using a step size of $d\omega = 0.02$ rad/s and $N = 100$. The wave energy spectrum for different significant wave heights is shown in Fig. 8(a) and justifies the range of frequency since almost all the energy is contained within $\omega_N = 2$ rad/s.

Using this discretization of the continuous spectrum along with uniformly distributed random phases ϵ_i on $[0, 2\pi]$, we generate a train of random waves that simulate the forcing due to the rough sea environment [19,30]. This is typically expressed as time-dependent angular accelerations in (1) and then rescaled using (9) to obtain random forcing. The form of time-dependent angular accelerations considered here is also treated in Refs. [31–33] and is given by

$$m_\phi(t) = \omega_\phi^2 \sin\chi\,\alpha_0 \frac{\sqrt{2d\omega}}{g} \sum_{i=1}^{N} \omega_i^2 \sqrt{S(\omega_i)} \sin\left(\frac{\omega_{ie}}{\omega_\phi} t + \epsilon_i\right) \tag{25}$$

$$m_\theta(t) = \omega_\theta^2 \cos\chi\,\alpha_0 \frac{\sqrt{2d\omega}}{g} \sum_{i=1}^{N} \omega_i^2 \sqrt{S(\omega_i)} \sin\left(\frac{\omega_{ie}}{\omega_\phi} t + \epsilon_i\right) \tag{26}$$

where t is the non-dimensional time measured in the units of natural roll frequency (2), ω_ϕ and ω_θ are the natural roll and pitch frequencies for a ship, χ is the heading angle of the waves with respect to the ship, α_0 is the effective wave slope being 0.73, ω_e is the encounter frequency (frequency experienced in the ship's reference frame) given by

$$\omega_e = \omega - \frac{\omega^2\, U}{g} \cos\chi \tag{27}$$

and U is the ship's speed. The heading angle and speed of the ship is illustrated in Fig. 1(b) along with different incident wave directions. We use the speed of the boat $U = 2.06$ m/s, and heading angle $\chi = 90^\circ$ (beam sea) in our simulations. In first order form, the equations of motion are given by (8) and the generalized time-dependent forcing is given by (9) and shown in Fig. 8(b).

In the phase space of $\xi = (x, y, v_x, v_y)$, that is $\mathbb{R}^4$, we classified trajectories that lead to capsize in absence of forcing in terms of the geometry of solutions near the equilibria (see Appendix B for details). We discovered the regions of the phase

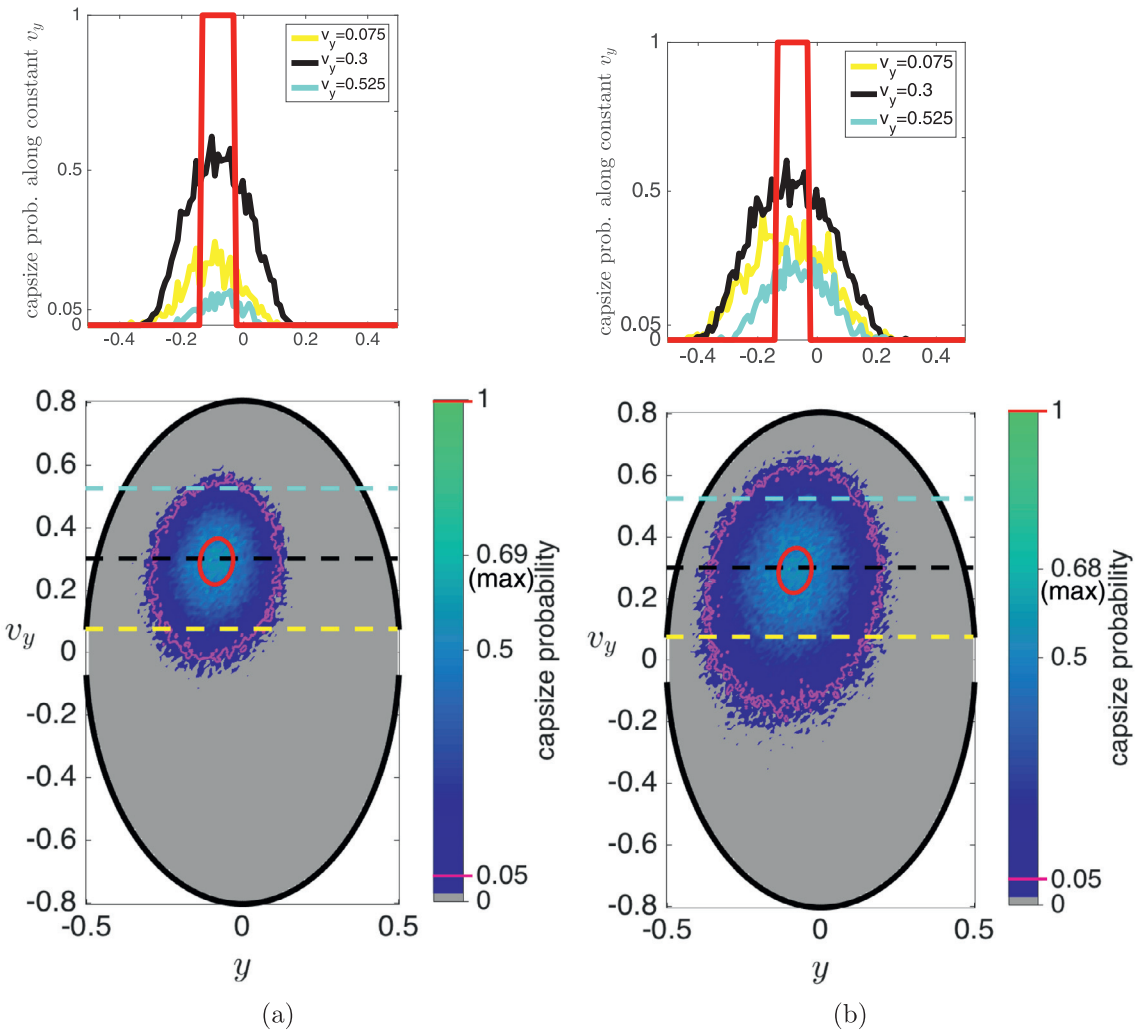

Fig. 9. (A) Shows the distribution of capsize probability as the contour plot with region that does not lead to capsize, that is starting conditions with 0 probability of imminent capsize, shown as grey region for $H_s = 4.92$ m and $\Delta E = 0.003$. (b) Shows the same for $H_s = 9.84$ m and $\Delta E = 0.003$. In both figures, the black boundary is the intersection of the energy ellipsoid (see Appendix E for details) with the Poincaré SOS and the magenta curve is the boundary of the region that has capsize probability greater than 0.05. In absence of random forcing, the boundary of the region with 1 probability is given by the tube intersection, shown as red curve. The dotted lines denote the cross-section of the distribution at a constant v_y, and shown at the top of the contour plot. The red bar of sharp unit probability corresponds to the tube intersection at its maximum width; while the spread out distribution correspond to the dotted lines with different v_y values. (For interpretation of the references to colour in this figure legend, the reader is referred to the web version of this article.)

space that lead to capsize through the bottleneck around critical points C_1 (right equilibrium point) or C_2 (left equilibrium point) as shown in Fig. 6. Now, we test the robustness of the tubes, a geometric structure in conservative dynamics, in presence of a random forcing. For simplifying the discussion, let us consider the case of imminent capsize for the critical point C_1, which in terms of tube dynamics means the first intersection of the stable manifold of C_1 with the SOS, U_1 (13).

In the conservative case, trajectories leading to imminent capsize via C_1 reside completely inside the boundary of intersection of the stable manifold of C_1 with SOS, U_1. Thus, in terms of capsize probability this means all the trajectories inside tube intersection have probability = 1 and all trajectories outside the tube have probability = 0. Now, if we consider rough seas in the form of wave forcing (9), each initial condition on the SOS U_1 generates an ensemble of realizations of the random dynamical system (8). When we consider a large number of these realizations (say, 400), each initial condition can be assigned a probability of capsize. This is simply the number of realizations that lead to capsize divided by the total number of realizations. Thus, we obtain a distribution of capsize probability for all starting conditions on the SOS, U_1, and is shown in the contour plot of Fig. 9 for $H_s = 4.92$ m and $H_s = 9.84$ m, when $\Delta E = 0.003$. This corresponds to a low total energy above the critical/escaping energy while the random forcing can be considered as moderate and high in terms of significant wave heights [19]. Furthermore, when we consider a higher total energy above the critical/escaping energy, we observe tube dynamics to be more prominent as the boundary now covers the region with higher capsize probability.

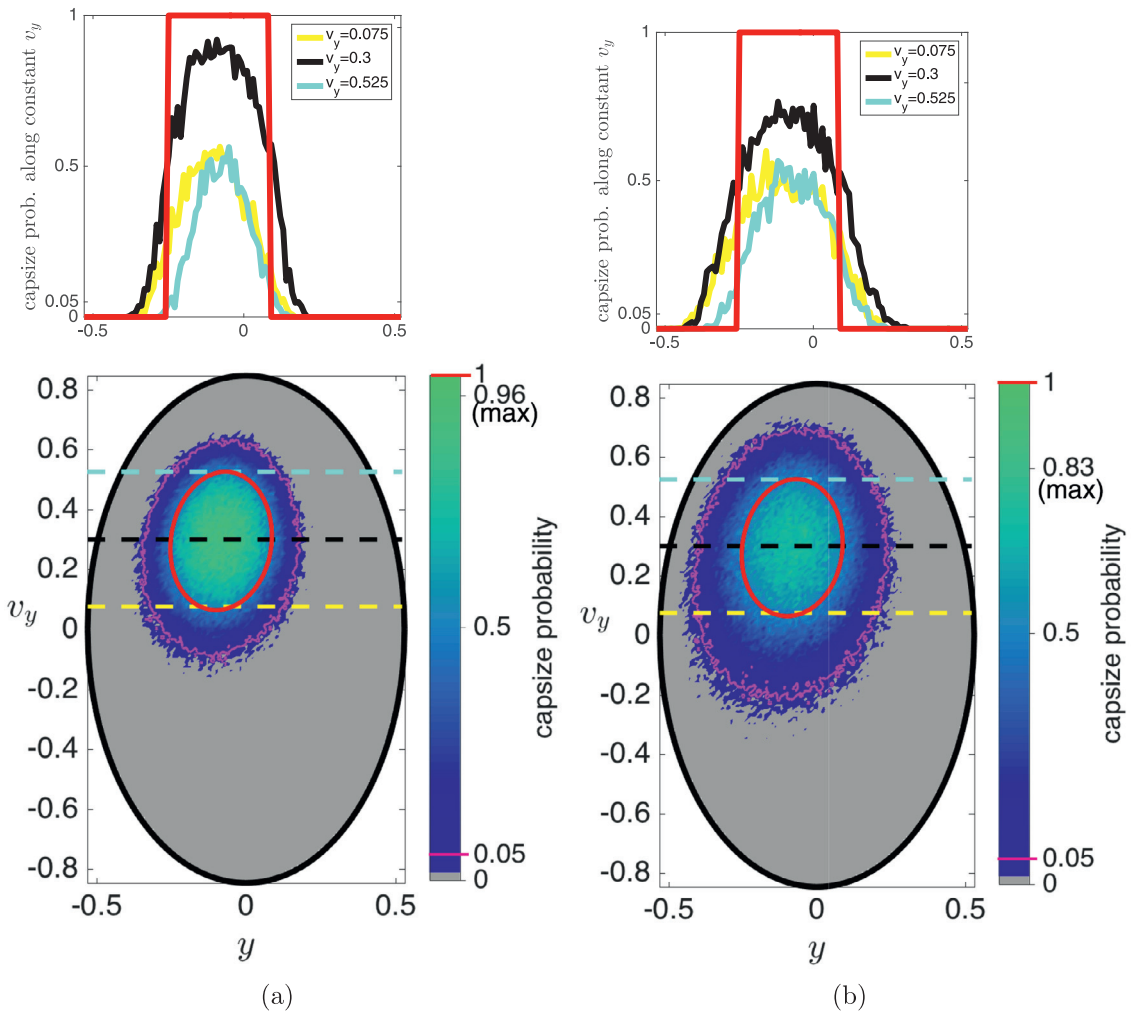

Fig. 10. (a) Shows the distribution of capsize probability as the contour plot with region that does not lead to capsize, that is starting conditions with 0 probability of imminent capsize, shown as grey region for $H_s = 4.92$ m and $\Delta E = 0.03$. (b) Shows the same for $H_s = 9.84$ m and $\Delta E = 0.03$.

The numerical demonstration shows that the tubes are robust to a general time-dependent forcing even though they are geometric structures derived from the conservative form. This is observed for both low and high total energy, as shown in Figs. 9 and 10, respectively, and also across moderate and high significant wave heights. Thus, the tube dynamics form the skeleton in predicting capsize probability even when random forcing is introduced. Thus, it provides a geometric framework to study escaping dynamics in presence of a general time-dependent forcing.

4. Discussion and conclusions

Ship motion exemplifies a field where the application of phase space transport to higher dimensions is sorely needed, but where a conceptual framework for dealing with multi-degree of freedom problems has been lacking [2,33]. Ship motion can be analytically modeled generally as a 6° of freedom system. Despite this, many models of ship dynamics focus on single-degree-of-freedom, reduced order models. But such models can be vulnerable to neglecting crucial dynamics. The ease of visualization of low dimensional dynamics has been part of their appeal. But couplings of multiple state variables can significantly alter predictions of safety versus capsize, as emphasized by Refs. [10,11,34], and thus 2 or more degrees of freedom should be included.

In this study, we attempted to introduce conceptual aids for multi-degree degree of freedom systems which may help in the interpretation of dynamics which lead to capsize.

Our approach was as follows.

- We considered first the dynamics of the underlying conservative system, which is itself non-trivial. These dynamics determine the phase space ‘skeleton’ upon which non-conservative forces, including random waves, are additional effects.

- In the simplest case of only two degrees of freedom, the phase space is of dimension four and the boundary between non-capsize and capsize states is given by a well-defined *transition state* (to use language borrowed from chemistry, but which has greater applicability [16,35,36]).
- The set of all states leading to capsize can be understood as residing within a hyper-cylindrical manifold or tube, as in Fig. 6. This tube is the set of all states which will soon reach the transition state [17,37]. From a probabilistic point of view, states in the tube will reach capsize with probability 1, while those outside have probability 0.
- With the addition of random wave forcing, the ensemble of trajectories leading to capsize is seen to be a smoothed probability distribution which shadows the underlying conservative system, as in as in Figs. 9 and 10. The peak probabilities match those from the conservative case. In the ensemble limit, small amplitude random waves are effectively noise, albeit bounded noise.
- However, this behavior also persists even for large amplitude random forcing (Figs. 9(b) and 10(b)), and hence provides a more general framework to study escaping dynamics.

An appealing aspect of this approach is that, while results for $N = 2$ degrees of freedom were shown for ease of discussion, the approach is completely scalable to higher degrees of freedom, as has been demonstrated in other contexts [36]. For example, when $N > 2$ the center manifold of bounded orbits (periodic and quasiperiodic orbits) has topology of $\mathbb{S}^{2N-3}$ and will need computation of their associated stable and unstable invariant manifolds. This is key, as it makes the approach attractive for the systematic analysis of multi-degree of freedom ship motions [2], up to and including all the degrees of freedom. Moreover, the tubes are also robust in the sense of predicting high probability regions of escape even in the presence of random forcing.

The foregoing study lays the foundation for a new approach to the avoidance of capsize. For instance, avoidance of capsize can be achieved by controlling a trajectory just enough to avoid entering the escaping zone on the surface-of-section. Future work on control will be forthcoming.

Acknowledgments

This work was supported in part by the National Science Foundation under awards 1150456, 1520825, and 1537349. The authors would like to thank Tom Battista, Michele Cooper, Leigh McCue, and Craig Woolsey for useful discussions and the reviewers for fruitful suggestions.

Appendix A. The linearized Hamiltonian system

The geometry of motion near the rank-1 saddle is explained by writing the Hamiltonian in its normal form which is obtained using a linear transformation and in this section, we present the details of this method. We note that the Hamiltonian for the rescaled system can be obtained via the usual Legendre transformation of the Lagrangian (4) and is given by

$$H(x, y, p_x, p_y) = \frac{1}{2}p_x^2 + \frac{1}{2}\left(\frac{R^2}{2}\right)p_y^2 + \frac{1}{2}x^2 + y^2 - x^2 y \tag{A.1}$$

We know the canonical form of the equations of motion in terms of the Hamiltonian for n degrees of freedom is given by

$$\begin{Bmatrix} \dot{\mathbf{q}} \\ \dot{\mathbf{p}} \end{Bmatrix} = J\nabla H \tag{A.2}$$

$$\text{where,} \quad J = \begin{bmatrix} 0_n & I_n \\ -I_n & 0_n \end{bmatrix} \tag{A.3}$$

is the symplectic $2n \times 2n$ matrix, $\{\mathbf{q}, \mathbf{p}\} = \{q_1, q_2, \ldots, q_n; p_1, p_2, \ldots, p_n\} \in \mathbb{R}^{2n}$ are the generalized coordinates, 0_n is the zero matrix of size $n \times n$, and I_n is the identity matrix of size $n \times n$. The equations of motion associated the Hamiltonian (A.1) are given by

$$\begin{aligned} \mathring{x} &= \frac{\partial H}{\partial p_x} = p_x \\ \mathring{y} &= \frac{\partial H}{\partial p_y} = \frac{R^2}{2}p_y \\ \mathring{p_x} &= -\frac{\partial H}{\partial x} = -x + 2xy \\ \mathring{p_y} &= -\frac{\partial H}{\partial y} = -2y + x^2 \end{aligned} \tag{A.4}$$

Eigenvalues and eigenvectors. The saddle equilibrium points are at (±1, 1/2, 0, 0) and the center equilibrium point is at (0, 0, 0, 0). The linearization of the equations of motion is given by

$$\mathbb{J}_{(x,y,p_x,p_y)} = \begin{bmatrix} 0 & 0 & 1 & 0 \\ 0 & 0 & 0 & R^2/2 \\ -1+2y & 2x & 0 & 0 \\ 2x & -2 & 0 & 0 \end{bmatrix} \tag{A.5}$$

which are evaluated at the equilibrium points (1, 1/2, 0, 0) becomes

$$\mathbb{J}_{(x,y,p_x,p_y)} = \begin{bmatrix} 0 & 0 & 1 & 0 \\ 0 & 0 & 0 & R^2/2 \\ 0 & 2 & 0 & 0 \\ 2 & -2 & 0 & 0 \end{bmatrix} = M \tag{A.6}$$

The characteristic polynomial is given by

$$\begin{aligned} p(\beta) = \det(M-\beta I) &= \begin{bmatrix} -\beta & 0 & 1 & 0 \\ 0 & -\beta & 0 & R^2/2 \\ 0 & 2 & -\beta & 0 \\ 2 & -2 & 0 & -\beta \end{bmatrix} \\ &= -\beta \begin{bmatrix} -\beta & 0 & R^2/2 \\ 2 & -\beta & 0 \\ -2 & 0 & -\beta \end{bmatrix} + 1 \begin{bmatrix} 0 & -\beta & R^2/2 \\ 0 & 2 & 0 \\ 2 & -2 & -\beta \end{bmatrix} \\ &= -\beta(-\beta(\beta^2-0)+R^2/2(0-2\beta)) + 1(\beta(0-0)+R^2/2(0-4)) \\ &= -\beta(-\beta^3 - 2\beta(R^2/3)) + (-2R^2) \\ p(\beta) &= \beta^4 + R^2\beta^2 - 2R^2 \end{aligned}$$

Let $\alpha = \beta^2$, then the roots of $p(\alpha) = 0$ are as follows

$$\alpha_1 = \frac{-R^2 + R\sqrt{8+R^2}}{2} \tag{A.7}$$

$$\alpha_2 = \frac{-R^2 - R\sqrt{8+R^2}}{2} \tag{A.8}$$

Since $R > 0$ always, being the ratio of frequencies, and the $\sqrt{8+R^2} > R$, we know $\alpha_1 > 0$ and $\alpha_2 < 0$. Thus, let us define $\lambda = \sqrt{\alpha_1}$ and $\nu = \sqrt{-\alpha_2}$.

Now, we want to find the eigenvectors of matrix (A.6) and use them to construct a symplectic linear change of variables which will cast (A.1) into its real normal form.

Let us assume the eigenvector to be $v = (k_1, k_2, k_3, k_4)$ and thus, $M\beta = \beta v$ gives the following equations:

$$\begin{aligned} k_3 &= \beta k_1 \\ \frac{R^2}{2} k_4 &= \beta k_2 \\ 2k_2 &= \beta k_3 \\ 2k_1 - 2k_2 &= \beta k_4 \end{aligned}$$

Let $k_1 = 1$, then the eigenvector has a form $(1, k_2, \beta, \frac{2\beta k_2}{R^2})$. Thus using the third and fourth equations for the eigenvalue $\beta = \lambda$ and $\beta = -\lambda$, we get

$$\begin{aligned} 2k_2 &= \lambda^2 \\ 1 - k_2 &= \frac{\lambda^2}{R^2} k_2 \\ 2k_2' &= (-\lambda)^2 \\ 1 - k_2' &= \frac{(-\lambda)^2}{R^2} k_2' \end{aligned}$$

which implies $k_2 = k_2'$ and let $k_2 = \sigma$, using the last equation we get

$$\sigma = \frac{R^2}{R^2 + \lambda^2} \tag{A.9}$$

Thus, using the third and fourth equations for the eigenvalue $\beta = i\nu$ and $\beta = -i\nu$, we get

$$\begin{aligned} 2k_2 &= -\nu^2 \\ 1 - k_2 &= -\frac{\nu^2}{R^2}k_2 \\ 2k_2' &= (-i\nu)^2 \\ 1 - k_2' &= \frac{(-i\nu)^2}{R^2}k_2' \end{aligned}$$

which again implies $k_2 = k_2'$ and let $k_2 = \tau$, using the last equation we get

$$\tau = \frac{2\nu}{R^2 - \nu^2}$$

Thus, the eigenvectors associated with eigenvalues $\pm\lambda$ becomes

$$\begin{aligned} u_\lambda &= \left[1, \frac{R^2}{R^2+\lambda^2}, \lambda, \frac{2\lambda}{R^2+\lambda^2}\right] \\ u_{-\lambda} &= \left[1, \frac{R^2}{R^2+\lambda^2}, -\lambda, -\frac{2\lambda}{R^2+\lambda^2}\right] \end{aligned}$$

and for the eigenvalue $i\nu$, we separate the real and imaginary parts as $u_\nu + iv_\nu$ to obtain the two eigenvectors

$$\begin{aligned} u_\nu &= \left[1, \frac{R^2}{R^2-\nu^2}, 0, 0\right] \\ v_\nu &= \left[0, 0, \nu, \frac{2\nu}{R^2-\nu^2}\right] \end{aligned}$$

Symplectic change of variables. Next, we consider the transformation given by the matrix C which is formed using the eigenvectors as the basis and is given by

$$C = [u_\lambda, u_\nu, -u_{-\lambda}, v_\nu] \tag{A.10}$$

To check whether this transformation is symplectic, that is the transformed Hamiltonian is in the normal form, we check the condition $C^T J C = J$ to obtain

$$C^T J C = \begin{bmatrix} 0_n & D \\ -D & 0_n \end{bmatrix} \quad \text{where,} \quad D = \begin{bmatrix} d_\lambda & 0 \\ 0 & d_\nu \end{bmatrix} \tag{A.11}$$

where 0_n is the zero matrix of size $n \times n$. The resulting structure can be obtained if we note that the factor $1 + \frac{2R^2}{(R^2-\nu^2)(R^2+\lambda^2)} = 0$ when the values of $\lambda = \sqrt{\alpha_1}$ and $\nu = \sqrt{-\alpha_2}$ is substituted from (A.7) and (A.8). Thus, the transformation matrix C is symplectic when scaled using the factors $s_1 = \sqrt{2d_\lambda}$ and $s_2 = \sqrt{d_\nu}$. These are given by

$$d_\lambda = \lambda + \frac{R^2}{R^2+\lambda^2}\frac{2\lambda}{R^2+\lambda^2} \tag{A.12}$$

$$d_\lambda = \nu + \frac{R^2}{R^2-\nu^2}\frac{2\nu}{R^2-\nu^2} \tag{A.13}$$

and it is easy to check $d_\lambda > 0$, $d_\nu > 0$. This implies that the final change is given by the symplectic transformation matrix C

$$\begin{bmatrix} 1/s_1 & 1/s_2 & -1/s_1 & 0 \\ \dfrac{R^2}{s_1(R^2+\lambda^2)} & \dfrac{R^2}{s_2(R^2-\nu^2)} & -\dfrac{R^2}{s_1(R^2+\lambda^2)} & 0 \\ \lambda/s_1 & 0 & \lambda/s_1 & \nu/s_2 \\ \dfrac{2\lambda}{s_1(R^2+\lambda^2)} & 0 & \dfrac{2\lambda}{s_1(R^2+\lambda^2)} & \dfrac{2\nu}{s_2(R^2-\nu^2)} \end{bmatrix} \tag{A.14}$$

which transforms the coordinates (x, y, p_x, p_y) into (q_1, q_2, p_1, p_2) and that casts Hamiltonian into its normal form given by

$$H(q_1, q_2, p_1, p_2) = \lambda q_1 p_1 + \frac{\nu}{2}(q_2^2 + p_2^2) \tag{A.15}$$

Thus, the linearized equations of motion near the saddle (1, 1/2, 0, 0) are

$$\begin{aligned} \mathring{q}_1 &= \lambda q_1 \qquad \mathring{p}_1 = -\lambda p_1 \\ \mathring{q}_2 &= \nu p_2 \qquad \mathring{p}_2 = -\nu q_2 \end{aligned} \tag{A.16}$$

and the solutions of the equations (A.16) is written as

$$q_1(t) = q_1^0 e^{\lambda t} \qquad p_1(t) = p_1^0 e^{-\lambda t} \quad q_2(t) + ip_2(t) = (q_2^0 + ip_2^0)e^{-i\nu t} \tag{A.17}$$

where the constants $q_1^0, p_1^0, q_2^0 + ip_2^0$ are the initial conditions. These linearized equations admit integrals in addition to the Hamiltonian function; namely, the functions $q_1 p_1$, $q_2^2 + p_2^2$ are constant along solutions.

Appendix B. Geometry of solutions near equilibria

The geometric view of the solutions near the equilibria, C_1 and C_2, is studied using the eigenbases for linearized equations of motion around these points. Let us consider the right equilibrium point, C_2, and the results for left equilibrium point, C_1, follows from symmetry, s_x.

Eigenvalues and eigenvectors. We compute the Jacobian of the vector field about this point and the linear system is now given by

$$\begin{pmatrix} \mathring{x} \\ \mathring{y} \\ \mathring{v}_x \\ \mathring{v}_y \end{pmatrix} = D\mathbf{f}|_{(x_e, y_e, 0, 0)} \begin{pmatrix} x \\ y \\ v_x \\ v_y \end{pmatrix} = \begin{bmatrix} 0 & 0 & 1 & 0 \\ 0 & 0 & 0 & 1 \\ 0 & 2 & 0 & 0 \\ R^2 & -R^2 & 0 & 0 \end{bmatrix} \begin{pmatrix} x \\ y \\ v_x \\ v_y \end{pmatrix} \tag{B.1}$$

for which the eigenvalues are obtained by solving the characteristic polynomial

$$\beta^4 + R^2\beta^2 - 2R^2 = 0 \tag{B.2}$$

Due to the simpler form of the above 4th order polynomial, the roots can be written as

$$\beta^2 = \frac{-R^2 \pm \sqrt{R^4 - 4(-2R^2)}}{2}$$

$$\beta = \pm \sqrt{\frac{R^2}{2}\left(-1 \pm \sqrt{1 + \frac{8}{R^2}}\right)}$$

Thus, the eigenvalues are of the form $\pm\lambda$ and $\pm i\nu$, where

$$\lambda = \sqrt{\frac{R^2}{2}\left(\sqrt{1 + \frac{8}{R^2}} - 1\right)} \qquad \nu = \sqrt{\frac{R^2}{2}\left(\sqrt{1 + \frac{8}{R^2}} + 1\right)} \tag{B.3}$$

These eigenvalues classify the equilibrium point C_2 (and C_1 due to symmetry s_x) as rank-1 saddle which, in general, means they possess one saddle direction and are center in all other directions. Thus, the eigenvectors corresponding to $\pm\lambda$ are of saddle type and the eigenvalues corresponding to $\pm i\nu$ are of center type that is periodic motion.

Let $v = (k_1, k_2, k_3, k_4)$ denote the eigenvector corresponding to the eigenvalue λ and the Jacobian matrix at C_2 is denoted by $A = D\mathbf{f}|_{(x_e, y_e, 0, 0)}$, then $Av = \alpha v$ gives

$$\begin{aligned} k_3 &= \lambda k_1 \qquad k_4 = \lambda k_2 \\ 2k_2 &= \lambda k_3 \qquad R^2(k_1 - k_2) = \lambda k_4 \end{aligned}$$

Let $k_1 = 1$, then using the first set of equations, the eigenvector is of the form $(1, k_2, \lambda, \lambda k_2)$ and we can solve λ, k_2 for different eigenvalues. For the real eigenvalues $\pm\lambda$, we obtain:

$$u_1 = \left(1, \frac{R^2}{R^2 + \lambda^2}, \lambda, \frac{\lambda R^2}{R^2 + \lambda^2}\right) \tag{B.4}$$

$$u_2 = \left(1, \frac{R^2}{R^2 + \lambda^2}, -\lambda, -\frac{\lambda R^2}{R^2 + \lambda^2}\right) \tag{B.5}$$

For the complex conjugate eigenvalues $\pm i\nu$, we obtain:

$$w_1 = \left(1, \frac{R^2}{R^2 - \nu^2}, i\nu, \frac{i\nu R^2}{R^2 - \nu^2}\right) \tag{B.6}$$

$$w_2 = \left(1, \frac{R^2}{R^2 - \nu^2}, -i\nu, -\frac{i\nu R^2}{R^2 - \nu^2}\right) \tag{B.7}$$

where, λ and ν are positive constants given by (B.3). Thus, the general solution of the linear system B.1 is given by

$$\mathbf{x}(t) = \{x(t), y(t), v_x(t), v_y(t)\} = \alpha_1 e^{\lambda t} u_1 + \alpha_2 e^{-\lambda t} u_2 + 2Re(\beta e^{i\nu t} w_1) \tag{B.8}$$

where, α_1, α_2 are real and $\beta = \beta_1 + i\beta_2$ is complex. However, we can use the eigenvectors to define a coordinate system that makes this picture more clearer.

Eigenvectors as axes for new coordinate system. To better understand the orbit structure on the phase space, we make a linear change of coordinates with the eigenvectors: u_1, u_2, w_1, w_2, as the axes of the new system. Using the corresponding new coordinates (ξ, η, ζ_1, ζ_2), the equations of motion near the equilibrium points assume the simple form:

$$\begin{aligned}
\dot{\xi} &= \lambda\xi \\
\dot{\eta} &= -\lambda\eta \\
\dot{\zeta}_1 &= \nu\zeta_2 \\
\dot{\zeta}_2 &= -\nu\zeta_1
\end{aligned} \tag{B.9}$$

and the energy integral for the linearized system becomes

$$E_l = \lambda\xi\eta + \frac{\nu}{2}\left(\zeta_1^2 + \zeta_2^2\right) \tag{B.10}$$

Thus, the solutions of the equations (B.9) can be written as

$$\begin{aligned}
\xi(t) &= \xi^0 \exp^{\lambda t} \\
\eta(t) &= \eta^0 \exp^{-\lambda t} \\
\zeta(t) &= \zeta_1(t) + i\zeta_2(t) = \zeta^0 \exp^{-i\nu t}
\end{aligned} \tag{B.11}$$

where, the constants ξ^0, η^0, and $\zeta^0 = \zeta_1^0 + i\zeta_2^0$ are the initial conditions. These linearized equations admit integrals in addition to the energy function (B.10); namely the functions $\xi\eta$ and $|\zeta|^2 = \zeta_1^2 + \zeta_2^2$ are both constant along solutions.

Local integrals in equilibrium region. The geometric view of solution near the equilibrium points is based on expressing the Hamiltonian in normal form which is based on Moser's Theorem. We present the discussion from [23] for the sake of completeness. Suppose we have a time-dependent, analytic Hamiltonian system of differential equations with two degrees of freedom. Suppose these equations have a non-degenerate equilibrium point with one pair of real and one pair of imaginary eigenvalues, $\pm\lambda$ and $\pm i\nu$. We can assume, without loss of generality, that the phase space coordinates (q_1, q_2, p_1, p_2) are chosen so that the Hamiltonian function assumes the following form:

$$H(q, p) = \lambda q_1 p_1 + \frac{\nu}{2}(q_2^2 + p_2^2) + \mathcal{O}_3(q, p),$$

where $q = (q_1, q_2)$, $p = (p_1, p_2)$ and the symbol $\mathcal{O}_n(\cdot, \cdot)$ denotes terms of order n or higher in the variables. In particular, the equilibrium point has coordinates $p = q = 0$ and the differential equations are obtained from H as

$$\begin{aligned}
\dot{q}_1 &= H_{p_1} = \lambda q_1 + \mathcal{O}_2(q, p) \\
\dot{q}_2 &= H_{p_2} = \nu p_2 + \mathcal{O}_2(q, p) \\
\dot{p}_1 &= -H_{q_1} = -\lambda p_1 + \mathcal{O}_2(q, p) \\
\dot{p}_2 &= -H_{q_2} = \nu q_2 + \mathcal{O}_2(q, p)
\end{aligned} \tag{B.12}$$

The linearized equations are similarly obtained from a Hamiltonian function which consists of the quadratic terms of H, or equivalently, by dropping the terms of order two or higher in the above equations. Solution of these linearized equations are conveniently written as

$$q_1(t) = q_1^0 e^{\lambda t} \qquad p_1(t) = p_1^0 e^{-\lambda t} \quad q_2(t) + ip_2(t) = (q_2^0 + ip_2^0)e^{-i\nu t} \tag{B.13}$$

where the constants q_1^0, p_1^0, and $q_2^0 + ip_2^0$ are the initial conditions. These linearized equations admit integrals in addition to the Hamiltonian function; namely, the functions $q_1 p_1$ and $q_2^2 + p_2^2$ are constant along solutions. A generalization of Lyapunov's theorem in [25] states that the full non-linear equations admit "local" integrals analogous to these via power series in q and p that start with quadratic terms $q_1 p_1$ and $q_2^2 + p_2^2$. It is also shown in [25] that the power series converges in some neighborhood of $q_1 = p_1 = 0$ and such that the corresponding functions are constants along pieces of solutions lying in the domain of convergence.

Moser's theorem. Let $q = p = 0$ correspond to a critical point as described above, then there exists a (real) analytic, transformation

$$\begin{aligned}
q_1 &= \xi + \mathcal{O}_2(\xi, \eta, \zeta, \bar{\zeta}), \\
p_1 &= \eta + \mathcal{O}_2(\xi, \eta, \zeta, \bar{\zeta}),
\end{aligned}$$

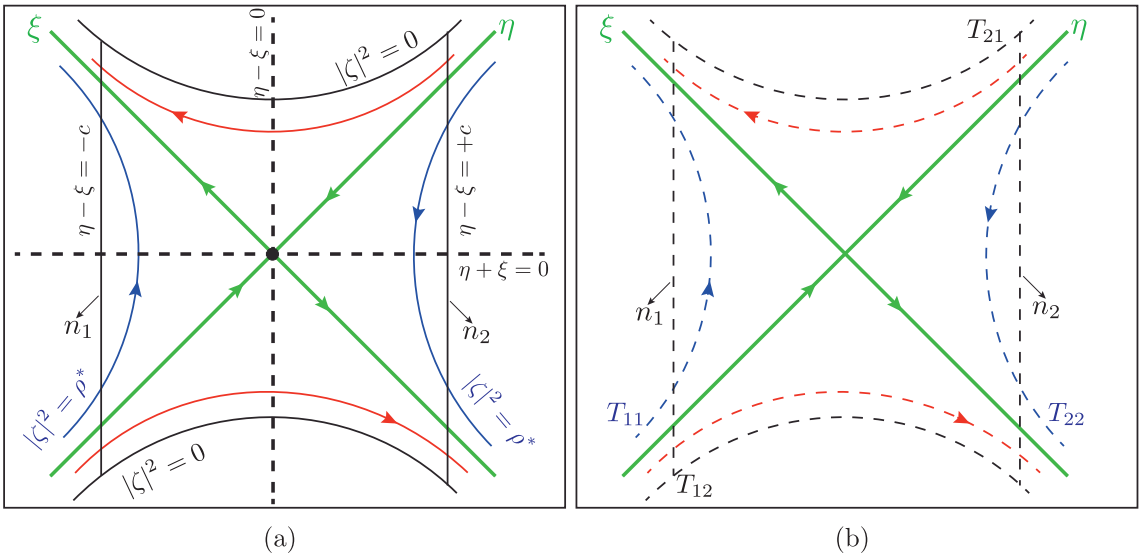

Fig. B.1. The projection onto the $\eta - \xi$ plane of orbits near the equilibrium point; the $\eta - \xi$ axis is rotated by 45°. (a) Shows the equilibrium region, $\mathcal{R}$, is bounded by the thick hyperbolic segments at top and bottom and the dotted vertical segments at left and right. At the origin is the periodic orbit in $\mathcal{R}$. The thick lines with arrows pointing toward or away from the origin are trajectories asymptotically winding onto the periodic orbit. (b) Shows four additional trajectories. The label T_{ij} denotes the path of a particle which entered $\mathcal{R}$ through n_i and exited through n_j. Two transit orbits, T_{12} and T_{21}, and two non-transit orbits, T_{11} and T_{22}, are shown.

$$q_2 + ip_2 = \zeta + \mathcal{O}_2(\xi, \eta, \zeta, \bar{\zeta}) \tag{B.14}$$

as well as power series α and β in the variables $\chi = \xi\eta$ and $|\zeta|^2$ of the form

$$\begin{aligned} \alpha &= \lambda + \mathcal{O}_1(\chi, |\zeta|^2) \\ \beta &= -i\nu + \mathcal{O}_1(\chi, |\zeta|^2) \end{aligned} \tag{B.15}$$

such that solutions of the transformed equations are given by

$$\begin{aligned} \xi(t) &= \xi^0 e^{t\alpha} \qquad \eta(t) = \eta^0 e^{-t\alpha} \\ \zeta(t) &= \zeta^0 e^{t\beta} \qquad \bar{\zeta}(t) = \bar{\zeta}^0 e^{-t\beta} \end{aligned} \tag{B.16}$$

where, ξ^0, η^0, and ζ^0 are determined from the initial conditions and $\bar{\zeta}$ is the complex conjugate of ζ. Furthermore, the coefficients of α and β are real and complex, respectively, from which it follows that the functions $\xi\eta = q_1 p_1 + \mathcal{O}_3(q, p)$ and $|\zeta|^2 = q_2^2 + p_2^2 + \mathcal{O}_3(q, p)$ are local integrals, as are α and β. Thus, the transformation of the Hamiltonian function has the form

$$\Gamma(\xi, \eta, \zeta, \bar{\zeta}) = H(q, p) = \lambda\xi\eta + \frac{1}{2}|\zeta|^2 + \mathcal{O}_2(\chi, |\zeta|^2) \tag{B.17}$$

and in particular depends only on the variables $\chi = \xi\eta$ and $|\zeta|^2$.

Flow in the equilibrium region. Consider a neighborhood of C_i, for $i = 1$ or $i = 2$ and fixed energy e, in the energy surface, then we refer to this neighborhood as the **equilibrium region** and denote it by $\mathcal{R}$ on the energy surface. The position space configuration will be denoted by R.

For positive e_l and c, the region $\mathcal{R}$, which is determined by

$$E_l = e_l \qquad \text{and,} \qquad |\eta - \xi| \leqslant c \tag{B.18}$$

which is homeomorphic to the product of a two-sphere and an interval; that is, for fixed value of $\eta - \xi$ on the interval $I = [-c, c]$, the equation $E_l = e_l$ defines the two-sphere

$$\frac{\lambda}{4}(\eta + \xi)^2 + \frac{\nu}{2}\left(\zeta_1^2 + \zeta_2^2\right) = e_l + \frac{\lambda}{4}(\eta - \xi)^2 \tag{B.19}$$

The bounding sphere of $\mathcal{R}$ for which $\eta - \xi = -c$ will be called n_1, and where $\eta - \zeta = c$, will be called n_2. We shall call the set of points on each bounding sphere where $\eta + \xi = 0$ as the *equator*, and the sets where $\eta + \xi > 0$ or $\eta + \xi < 0$ will be called the *north* and *south* hemispheres, respectively.

To analyze the flow in $\mathcal{R}$ one simply considers the projections on the $\eta - \xi$ plane and ζ planes, respectively. In the first case, we see the standard picture of an unstable equilibrium point, and in the second, of a center. Fig. B.1 illustrates the flow in the $\eta - \xi$ plane with the coordinate axes tilted by 45°. In Fig. B.1(b), $\mathcal{R}$ itself projects to a set bounded on two sides

by the hyperbola $\eta - \xi = e/\lambda$, denoted by thick solid hyperbolic segments on the top and bottom. $\mathcal{R}$ is bounded on two other two sides by the line segments $\eta - \xi = \pm c$, denote by dotted vertical lines on the left and right, which correspond to the bounding spheres , n_1 and n_2, respectively. Since $\eta\xi$ is an integral of the equations in $\mathcal{R}$, the projections of orbits in the $\eta - \xi$ plane move on the branches of the corresponding hyperbolas $\eta\xi = e/\lambda$, except in the case $\eta\xi = 0$. If $\eta\xi > 0$, the branches connect the bounding line segments $\eta - \xi = \pm c$ and if $\eta\xi < 0$, they have both end points on the same segment. A check of equation (B.16) shows that the orbits move as indicated by the arrows in Fig. B.1.

To interpret Fig. B.1 as a flow in $\mathcal{R}$, notice that each point in the projection corresponds to a circle in $\mathcal{R}$ given by the "radius" variable $\rho = |\zeta|^2 =$ constant. We recall from (B.10) that $|\zeta|^2 = \frac{2}{\nu}(e - \lambda\eta\xi)$ and for points on the bounding hyperbolic segments $\eta - \xi = e/\lambda$, the constant is zero so that the circle collapses to a point. Thus, the segments of the lines $\eta - \xi = \pm c$ in the $\eta - \xi$ projection correspond to the two-spheres bounding $\mathcal{R}$. Since each corresponds to a circle crossed with an interval where the two end circles are pinched to a point.

Thus, we can distinguish between nine classes of orbits grouped into four categories:

1. The point at the origin in Fig. B.1(a), $\xi = \eta = 0$, corresponds to a periodic orbit in $\mathcal{R}$
2. The four half-open segments on the axes, $\eta\xi = 0$ (or equivalently $|\zeta|^2 = \rho^*$ where $\rho^* = 2e/\nu$), correspond to four cylinders of orbits asymptotic to this periodic solution either as time increases ($\xi = 0$) or as time decreases ($\eta = 0$). These are called asymptotic orbits. These are drawn as the solid green lines with arrows pointing toward or away from the origin in Fig. B.1.
3. The hyperbolic segments determined by $\eta\xi =$constant > 0 (or equivalently $|\zeta|^2 < \rho$) correspond to two cylinders which cross $\mathcal{R}$ from one bounding sphere to the other, meeting both in the same hemisphere; the north one if they go from $\eta - \xi = +c$ to $\eta - \xi = -c$, the south one in the other case. Since these orbits transit from one region to another, we call them transit orbits. The two trajectories labeled T_{12} and T_{21} in Fig. B.1(b).
4. Finally, the hyperbolic segments determined by $\eta\xi =$constant < 0 ($|\zeta|^2 > \rho^*$) correspond to two cylinders of orbits in $\mathcal{R}$ each of which runs from one hemisphere to the other hemisphere on the same bounding sphere. Thus if $\eta > 0$, the sphere is n_1 ($\eta - \xi = -c$) and orbits run from the south ($\eta + \xi < 0$) to the north ($\eta + \xi > 0$) hemisphere while the converse holds if $\eta < 0$, where the sphere is n_2. Since these orbits return to the same region, we call them non-transit orbits. These two trajectories are labeled T_{11} and T_{22} in Fig. B.1(b).

Appendix C. Derivation of coupling constant

For applying the methods developed for 1 DOF and 2 DOF model of ship dynamics, we need to estimate the ratio of second moment of inertia and the coupling constant for the ship, *Edith Terkol*. The ratio of pitch and roll natural frequencies is given by R, so we have

$$\omega_\theta = R\omega_\phi \tag{C.1}$$

Furthermore, we know the angle of vanishing stability, ϕ_e and the corresponding pitch angle, θ_e is given by

$$\phi_e = \frac{\omega_\phi \omega_\theta}{K_1\sqrt{2}}\sqrt{\frac{I_{yy}}{I_{xx}}}, \qquad \theta_e = \frac{\omega_\phi^2}{2K_1}$$

Thus, we have

$$\theta_e = \frac{K_1}{\omega_\theta^2}\frac{I_{xx}}{I_{yy}}\phi_e^2$$

Let us consider the equation of motion for roll degree of freedom and its nonlinear term involving K_1 in (1) for the angle of vanishing stability. So we have

$$\begin{aligned} 2K_1\theta_e\phi_e &= 2K_1\phi_e\left(\frac{K_1}{\omega_\theta^2}\frac{I_{xx}}{I_{yy}}\phi_e^2\right) = \frac{2K_1^2}{\omega_\theta^2}\frac{I_{xx}}{I_{yy}}\phi_e^3 \\ &= \frac{2K_1^2}{R^2\omega_\phi^2}\frac{I_{xx}}{I_{yy}}\phi_e^3 \\ &= A\phi_e^3 \end{aligned}$$

Thus, the restoring moment (in terms of potential energy $V(\phi)$ this is $-\frac{dV}{d\phi}$) for roll dynamics is given by

$$M_\phi = -\omega_\phi^2\phi + A\phi^3 = \phi\left(-\omega_\phi^2 + A\phi^2\right) \tag{C.2}$$

which vanishes at instant of capsize, $\phi = \phi_e$. Thus, we have

$$A = \omega_\phi^2/\phi_e^2 \tag{C.3}$$

and for the ship *Edith Terkol*, $A = 0.5239$ s^{-2}. Thus, computing the constant K_1 requires estimating the ratio of second moment of inertia assuming a solid rectangular parallelepiped. Using $L = 58.6$ m, $B = 9.65$ m, and $D = 4.15$ m (as shown in

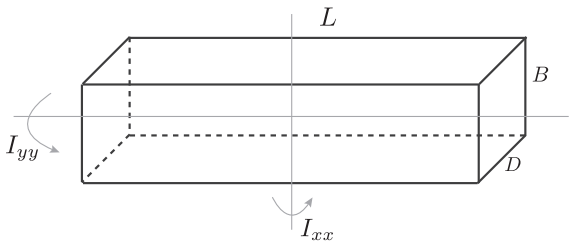

Fig. C.1. Schematic of a solid rectangular parallelepiped that represents a ship.

Fig. C.1) from Ref. [38] and the formula for I_{xx} and I_{yy}, we get

$$I_{xx} = \frac{m}{12}\left(D^2 + B^2\right)$$

and,

$$I_{yy} = \frac{m}{12}\left(L^2 + D^2\right)$$

which gives

$$\frac{I_{yy}}{I_{xx}} = \frac{L^2 + D^2}{B^2 + D^2} \tag{C.4}$$

which on substitution of appropriate values gives 31.28. Thus, the coupling constant is given by

$$K_1 = \sqrt{\frac{A\omega_\phi^2}{2}\frac{I_{yy}}{I_{xx}}R} \tag{C.5}$$

Appendix D. Derivation of differential correction term

Let trajectories of the differential equation $\dot{x} = f(x)$, e.g. (6), with initial condition $x(t_0) = x_0$ be denoted by the flow map $\phi(t,\, t_0;\, x_0)$, or $\phi(t;\, x_0)$. In what follows, we note $x \in \mathbb{R}^n$ and $f : \mathbb{R}^n \to \mathbb{R}^n$ unless the specific case of $n = 4$ for 2 ° of freedom systems is mentioned. For the guess initial condition, $\bar{x}_{0,g}$, a first guess to an initial condition along a periodic orbit, a trajectory that starts from the perturbed initial vector $\bar{x}_0 + \delta\bar{x}_0$ evolved until $t + \delta t$ with the displacement

$$\delta\bar{x}(t + \delta t) = \phi(t + \delta t, t_0; \bar{x}_0 + \delta\bar{x}_0) - \phi(t, t_0; \bar{x}_0)$$

with respect to the first guess reference solution $\bar{x}(t)$. We compute the displacement at time $t_1 + \delta t_1$ using

$$\delta\bar{x}(t_1 + \delta t_1) = \phi(t_1 + \delta t_1, t_0; \bar{x}_0 + \delta\bar{x}_0) - \phi(t_1, t_0; \bar{x}_0) \tag{D.1}$$

and expanding the right hand side using Taylor series, we get

$$\delta\bar{x}(t_1 + \delta t_1) = \frac{\partial\phi(t_1, t_0; \bar{x}_0)}{\partial x_0}\delta\bar{x}_0 + \frac{\partial\phi(t_1, t_0; \bar{x}_0)}{\partial t_1}\delta t_1 + h.o.t, \tag{D.2}$$

$$= \frac{\partial\phi(t_1, t_0; \bar{x}_0)}{\partial x_0}\delta\bar{x}_0 + \dot{\bar{x}}_1\delta t_1 + h.o.t, \tag{D.3}$$

where the first part of the second term $\frac{\partial\phi(t_1,t_0;\bar{x}_0)}{\partial t_1}$ comes from $\frac{d\phi(t,t_0;\bar{x}_0)}{dt} = f(\phi(t, t_0; \bar{x}_0))$, which is the vector field after flowing for $t = t_1$ along the reference trajectory. The matrix, $\frac{\partial\phi(t_1,t_0;\bar{x}_0)}{\partial t_1}$, which satisfies the above relation to first order $\delta t_1 = 0$ is the state transition matrix (STM) denoted by $\Phi(t_1, t_0)$. The first term involving the derivative of a trajectory with respect to the initial condition at $t = t_1$ is given by

$$\delta\bar{x}(t_1) = \Phi(t_1, t_0)\delta\bar{x}_0$$

can be obtained numerically as a solution to the variational equations

$$\delta\dot{\bar{x}}(t) = Df(\bar{x}(t))\delta\bar{x} \tag{D.4}$$

where $Df(\bar{x}(t))$ is the Jacobian of the vector field evaluated at $\bar{x}(t)$. Suppose we want to reach a desired endpoint, x_d, but

$$\bar{x}(t_1) = \phi(t_1, t_0; \bar{x}_0) = \bar{x}_1 = x_d - \delta\bar{x}_1$$

is slightly off ($|\delta\bar{x}_1| > d$) for a specified tolerance $d \ll 1$ and we need correction. Since,

$$\begin{aligned}\phi(t_1, t_0; \bar{x}_0 + \delta\bar{x}_0) &= \phi(t_1, t_0; \bar{x}_0) + \frac{\partial\phi(t_1, t_0; \bar{x}_0)}{\partial x_0}\delta\bar{x}_0 + h.o.t.,\\ &= \phi(t_1, t_0; \bar{x}_0) + \Phi(t_1, t_0)\delta\bar{x}_0 + h.o.t.,\\ &= \bar{x}_1 + \delta\bar{x}_1 + h.o.t.,\\ &= x_d + h.o.t.,\end{aligned}$$

which implies that changing $\bar{x}_0$ by

$$\delta\bar{x}_0 = \Phi(t_1, t_0)^{-1}\delta\bar{x}_1$$

will perform the correction to first order. By iteration, the process converges with the criteria:

$$\|\phi(t_1, t_0; \bar{x}_0 + \Delta\bar{x}_0) - x_d\| < d$$

where $\Delta\bar{x}_0$ is the accumulation of corrections $\delta\bar{x}_0$ which yields x_d within the desired tolerance d. Thus, the procedure of differential correction proceeds as follows:

We choose a guess initial condition, $\bar{x}_{0,g}$ at $t_0 = 0$, for example this is of the form $[x_0, y_0, 0, 0]^T$ for the roll-pitch coupled model (22).

Using a high tolerance (typically 10^{-14}) for a standard integration package, we integrate this initial condition until the *half-period event* is satisfied. This gives us $\bar{x}(t_1)$, so we can compute $\Phi(t_1, 0)$ and for a periodic orbit, the desired final state has the form

$$\bar{x}(t_1) = [x_1, y_1, 0, 0]^T$$

where, $t_1 = T/2$, a *half-period* of the periodic orbit. As a result of numerical integration, the obtained value of v_{x_1} may not be 0 and for our purpose of convergence, we want $|v_{x_1}| < d$ (for example, $d = 10^{-10}$). Thus, the state transition matrix after one half-cycle, $\Phi(t_1, 0)$, can be used to correct the initial condition to obtain a periodic orbit as

$$\delta\bar{x}_1 \approx \Phi(t_1, 0)\delta\bar{x}_0 + \dot{\bar{x}}_1\delta t_1$$

Suppose $|v_{x_1}| > d$ and we keep x_0 constant, then expanding the above linear system, the correction to v_{y_0} can be calculated from

$$\begin{aligned}v_{x_1} &= \delta v_{x_1} = \Phi_{32}\delta y_0 + \dot{v}_{x_1}\delta t_1 + h.o.t.\\ 0 &= \delta v_{y_1} = \Phi_{42}\delta y_0 + \dot{v}_{y_1}\delta t_1 + h.o.t\end{aligned}$$

where, $\Phi_{i,j}$ is an element of the matrix $\Phi(t_1, 0)$ and $\dot{v}_{x_1}$ comes from the equations of motion evaluated at the *half-period event*, $t = t_1$. Here, we set $v_{x_1} = \delta v_{x_1}$ to enforce $v_{x_1} = 0$. Furthermore, eliminating δt_1, we get

$$\delta t_1 = -\frac{\Phi_{42}\delta y_0}{\dot{v}_{y_1}}$$

and substituting in the equation for correction to δv_{x_1}, we get

$$\begin{aligned}v_{x_1} &= \Phi_{32}\delta y_0 + \dot{v}_{x_1}\left(-\Phi_{42}\frac{\delta y_0}{\dot{v}_{y_1}}\right)\\ v_{x_1} &= \delta y_0\left(\Phi_{32} - \Phi_{42}\frac{\dot{v}_{x_1}}{\dot{v}_{y_1}}\right)\end{aligned}$$

and hence the y-coordinate should be corrected by

$$\delta y_0 = \left(\Phi_{32} - \Phi_{42}\frac{\dot{v}_{x_1}}{\dot{v}_{y_1}}\right)^{-1} v_{x_1} \tag{D.5}$$

Thus, the differential correction in one of the coordinates can be used to correct the guess for initial condition of a periodic orbit. This can be adopted as a general numerical procedure for unstable periodic orbits or unstable solutions of differential equations with known end points.

Appendix E. Boundary of total energy on surface-of-section

The energy surface given by (12) can be visualized as an ellipsoid in the (y, v_y, v_x)-space. When $x = 0$, that is the intersection with the surface-of-section, U_1 (13) or (14), the total energy (12) becomes

$$E(x, y, v_x, v_y) = e = \frac{y^2}{1} + \frac{v_y^2}{R^2} + \frac{v_x^2}{2} \tag{E.1}$$

$$\frac{y^2}{(\sqrt{e})^2} + \frac{v_y^2}{(R\sqrt{e})^2} + \frac{v_x^2}{(\sqrt{2e})^2} = 1 \tag{E.2}$$

Now, the boundary of energetically accessible region on the surface-of-section, U_1 or U_2, is given by $v_x = 0$. Thus the boundary of constant total energy is the ellipse

$$\frac{y^2}{(\sqrt{e})^2} + \frac{v_y^2}{(R\sqrt{e})^2} = 1 \tag{E.3}$$

with $2R\sqrt{e}$ as major axis and $2\sqrt{e}$ as minor axis for $R > 1$.

References

[1] Soliman MS, Thompson JMT. Transient and steady state analysis of capsize phenomena. Appl Ocean Res 1991;13(2):82–92.
[2] Spyrou KJ, Thompson JMT. The nonlinear dynamics of ship motions: a field overview and some recent developments. Philosoph Trans R Soc A 2000;358(1771):1735–60.
[3] Thompson JMT, Soliman MS. Fractal control boundaries of driven oscillators and their relevance to safe engineering design. Proc R Soc A 1990;428(1874):1–13.
[4] Lin H, Yim SCS. Chaotic roll motion and capsize of ships under periodic excitation with random noise. Appl Ocean Res 1995;17(3):185–204.
[5] Falzarano JM, Shaw SW, Troesch AW. Application of global methods for analyzing dynamical systems to ship rolling motion and capsizing. Int J Bifurcation Chaos 1992;2:101–15.
[6] Paulling JR, Rosenberg RM. On unstable ship motions resulting from nonlinear coupling. J Ship Res 1959;3:36–46.
[7] Nayfeh AH, Mook DT, Marshall LR. Nonlinear coupling of pitch and roll modes in ship motions. J Hydronautics 1973;7(4):145–52.
[8] Nayfeh AH, Mook DT, Marshall LR. Perturbation-Energy approach for the development of the nonlinear equations of ship motion. J Hydronautics 1974;8(4):130–6.
[9] Mook DT, Marshall LR, Nayfeh AH. Subharmonic and superharmonic resonances in the pitch and roll modes of ship motions. J Hydronautics 1974;8(1):32–40.
[10] McCue LS, Troesch AW. The effect of coupled heave/heave velocity or sway/sway velocity initial conditions on capsize modeling. In: Proceedings of the 8th international conference on stability of ships and ocean vehicles, Madrid, Spain; 2003. p. 521–9.
[11] McCue L, Troesch A. Probabilistic determination of critical wave height for a multi-degree of freedom capsize model. Ocean Eng 2005;32(13):1608–22.
[12] McCue L, Bassler C, Belknap W. Real-time Identification of Behavior Leading to Capsize. In: Proceedings of the 9th International Conference on Stability of Ships and Ocean Vehicles, Rio de Janeiro, Brazil; 2006.
[13] Barrio R, Blesa F, Serrano S. Bifurcations and safe regions in open hamiltonians. New J Phys 2009;11(5):053004.
[14] Neves MA, Rodríguez CA. On unstable ship motions resulting from strong non-linear coupling. Ocean Eng 2006;33(14–15):1853–83.
[15] Neves MA, Rodríguez CA. A coupled non-linear mathematical model of parametric resonance of ships in head seas. Appl Math Model 2009;33(6):2630–45.
[16] Jaffé C, Ross S, Lo M, Marsden J, Farrelly D, Uzer T. Statistical theory of asteroid escape rates. Phys Rev Lett 2002;89(1):011101.
[17] Koon WS, Lo MW, Marsden JE, Ross SD. Heteroclinic connections between periodic orbits and resonance transitions in celestial mechanics. Chaos (Woodbury, NY) 2000a;10(2):427–69.
[18] Koon W-S, Marsden JE, Ross SD, Lo M, Scheeres DJ. Geometric mechanics and the dynamics of asteroid pairs. Ann N Y Acad Sci 2004;1017:11–38.
[19] Perez T. Ship Motion Control. Advances in Industrial Control. London: Springer-Verlag; 2005. chap. 2
[20] Thompson JMT, Souza JRD. Suppression of escape by resonant modal interactions: in shell vibration and heave-Roll capsize. Proc R Soc A 1996;452(1954):2527–50.
[21] Sepulveda MA, Heller EJ. Semiclassical analysis of hierarchical spectra. J Chem Phys 1994;101(9):8016.
[22] Babyuk D, Wyatt RE, Frederick JH. Hydrodynamic analysis of dynamical tunneling. J Chem Phys 2003;119(13):6482.
[23] Koon WS, Lo MW, Marsden JE, Ross SD. Dynamical systems, the three-body problem and space mission design; 2011. Marsden Books, ISBN 978-0-615-24095-4.
[24] Gómez G, Koon WS, Lo MW, Marsden JE, Masdemont JJ, Ross SD. Connecting orbits and invariant manifolds in the spatial restricted three-body problem. Nonlinearity 2004;17.5:1571–606.
[25] Moser J. On the generalization of a theorem of a. liapounoff. Commun Pure Appl Math 1958;XI:257–71.
[26] MacKay RS, Strub DC. Bifurcations of transition states: morse bifurcations. Nonlinearity 2015;28:4303–29.
[27] Meyer KR, Hall GR, Offin D. Introduction to hamiltonian dynamical systems and the N-Body problem. Springer; 2009. ISBN 9780387097237.
[28] Koon WS, Lo MW, Marsden JE, Ross SD. Heteroclinic connections between periodic orbits and resonance transitions in celestial mechanics. Chaos (Woodbury, NY) 2000b;10(2):427–69.
[29] Marsden JE, Ross SD. New methods in celestial mechanics and mission design. Bull Am Math Soc 2006;43(1):43–73.
[30] Perez T, Blanke M. Ship roll motion control. In: Proceedings of the 8th IFAC conference on control applications in marine systems, Rostock, Germany; 2010. p. 1–12.
[31] Senjanovic I, Cipric G, Parunov J, Senjanovic j, Cipric I, Parunov G J. Survival analysis of fishing vessels rolling in rough seas. Philosoph Trans 2000;358(1771):1943–65.
[32] Jiang C, Troesch AW, Shaw SW. Capsize criteria for ship models with memory-dependent hydrodynamics and random excitation. Philosoph Trans R Soc A 2000;358(1771):1761–91.
[33] Hsieh S-R, Troesch AW, Shaw SW. A nonlinear probabilistic method for predicting vessel capsizing in random beam seas. Proc R Soc A 1994;446(1926):195–211.
[34] Lee Y-W, McCue LS, Obar MS, Troesch AW. Experimental and numerical investigation into the effects of initial conditions on a three degree of freedom capsize model. J Ship Res 2006;50.1:63–84.
[35] Jaffé C, Farrelly D, Uzer T. Transition state in atomic physics. Phys Rev A 1999;60(5):3833–50.
[36] Gabern F, Koon WS, Marsden JE, Ross SD. Theory and computation of non-RRKM lifetime distributions and rates in chemical systems with three or more degrees of freedom. Physica D 2005;211(3–4):391–406.
[37] Gabern F, Koon WS, Marsden JE, Ross SD, Yanao T. Application of tube dynamics to non-statistical reaction processes. Few Body Syst 2006;38(2–4):167–72.
[38] White AS, Gleeson PT, Karamanoglu M. Control of ship capsize in stern quartering seas. Int J Simul Syst Sci Technol 2007;8(2):20–31.